Experimental Observation of Thermalization with Noncommuting Charges

Florian Kranzl[1,2,‡] Aleksander Lasek,[3,‡] Manoj K. Joshi[1] Amir Kalev,[4] Rainer Blatt,[1,2]
Christian F. Roos[1,2,*] and Nicole Yunger Halpern[3,5,6,7,†]

[1]*Institut für Quantenoptik und Quanteninformation, Österreichische Akademie der Wissenschaften,
Technikerstraße 21a, Innsbruck 6020, Republic of Austria*
[2]*Institut für Experimentalphysik, Universität Innsbruck, Technikerstraße 25, Innsbruck 6020, Republic of Austria*
[3]*Joint Center for Quantum Information and Computer Science, National Institute of Standards and Technology
(NIST) and University of Maryland, College Park, Maryland 20742, USA*
[4]*Information Sciences Institute, University of Southern California, Arlington, Virginia 22203, USA*
[5]*Institute for Physical Science and Technology, University of Maryland, College Park, Maryland 20742, USA*
[6]*ITAMP, Harvard-Smithsonian Center for Astrophysics, Cambridge, Massachusetts 02138, USA*
[7]*Department of Physics, Harvard University, Cambridge, Massachusetts 02138, USA*

Quantum simulators have recently enabled experimental observations of the internal thermalization of quantum many-body systems. Often, the global energy and particle number are conserved and the system is prepared with a well-defined particle number—in a microcanonical subspace. However, quantum evolution can also conserve quantities, or charges, that fail to commute with each other. Noncommuting charges have recently emerged as a subfield at the intersection of quantum thermodynamics and quantum information. Until now, this subfield has remained theoretical. We initiate the experimental testing of its predictions, with a trapped-ion simulator. We prepare 6–21 spins in an approximate microcanonical subspace, a generalization of the microcanonical subspace for accommodating noncommuting charges, which cannot necessarily have well-defined nontrivial values simultaneously. We simulate a Heisenberg evolution using laser-induced entangling interactions and collective spin rotations. The noncommuting charges are the three spin components. We find that small subsystems equilibrate to near a recently predicted non-Abelian thermal state. This work bridges quantum many-body simulators to the quantum thermodynamics of noncommuting charges, the predictions of which can now be tested.

I. INTRODUCTION

Thermalization aims the arrow of time, yet has traditionally been understood through the lens of classical systems. An understanding of quantum thermalization is therefore of fundamental importance. Quantum simulator experiments have recently elucidated how closed quantum many-body systems thermalize internally [1–4]. Typically, the evolutions conserve no quantities (as in gate-based evolutions) or conserve the energy and the particle number (in analog quantum simulators). The conserved quantities, called *charges*, are represented by Hermitian operators $Q_{\gamma=1,2,...,c}$. The operators are usually assumed implicitly to commute with each other, as do the commonly conserved Hamiltonian and particle-number operator. Yet noncommuting operators underlie quantum physics from uncertainty relations to measurement disturbance. What happens if thermodynamic charges fail to commute with each other? This question has recently swept across quantum thermodynamics [5–39] and infiltrated many-body theory [14,19–24,33,38–40]. We initiate experimentation on thermalization in the presence of noncommuting charges.

A many-body system thermalizes internally as a small subsystem $\mathcal{S}$ approaches the appropriate thermal state, which depends on the charges. The rest of the global system acts as an effective environment. Arguments for the form of the thermal state rely implicitly on commutation of the charges [6,8,21,41]. For example, the eigenstate-thermalization hypothesis explains the internal thermalization of quantum many-body systems governed by nondegenerate Hamiltonians [42–44]—yet

*christian.roos@uibk.ac.at
†nicoleyh@umd.edu
‡The first two coauthors contributed equally.

noncommuting charges imply energy degeneracies. Therefore, whether $\mathcal{S}$ can even thermalize, if charges fail to commute with each other, is not obvious.

Information-theoretic arguments suggest that $\mathcal{S}$ equilibrates to near a state dubbed the *non-Abelian thermal state* (NATS) [6–9,45],

$$\rho_{\text{NATS}} := \exp\left(-\beta\left[H - \sum_{\gamma=1}^{c}\mu_\gamma Q_\gamma\right]\right)/Z_{\text{NATS}}, \quad (1)$$

where β denotes the inverse temperature, H denotes the Hamiltonian of $\mathcal{S}$, the μ_γ denote effective chemical potentials, the Q_γ denote the c nonenergy charges of $\mathcal{S}$, and the partition function Z_{NATS} normalizes the state. States of the form given in Eq. (1) are also called *generalized Gibbs ensembles*, especially if the charges commute and the global Hamiltonian is integrable [46–48]. ρ_{NATS} has the exponential form typical of thermal states. Since the Q_γ fail to commute, however, two common derivations of the form of the thermal state break down [6,8]. For this reason, we distinguish ρ_{NATS} by the term *non-Abelian*. Arguments for Eq. (1) center on information theory, kinematics, and idealizations, such as a very large system-and-environment composite [7–9,45]. Whether $\mathcal{S}$ thermalizes outside these idealizations, under realistic dynamics, has remained unclear. Whether experimentalists can observe ρ_{NATS} has remained even less clear. Experimental control is finite, so no quantum many-body system is truly closed. If many species of charge can leak out, many conservation laws can be violated.

Beyond these practicalities, the extent to which noncommuting charges permit thermalization has been fundamentally unclear. If just energy and particle number are conserved, then, to thermalize $\mathcal{S}$, we prepare the global system in a *microcanonical subspace*: in a narrow energy window in a particle-number sector [49]. If more charges are conserved, the microcanonical subspace is a joint eigenspace shared by the c global charges. If the charges fail to commute, they share no eigenbasis, so they may share no eigenspace: no microcanonical subspace necessarily exists. To accommodate noncommuting charges [8], microcanonical subspaces have been generalized to *approximate microcanonical (AMC) subspaces*. In an AMC subspace, measuring any global charge has a high probability of yielding the expected value. The uncertainty in the initial values of the global charges may generate uncertainty in the long-time state of $\mathcal{S}$: $\mathcal{S}$ may remain farther from ρ_{NATS} than it would remain from the relevant thermal state if the charges commuted [21]. Furthermore, if charges fail to commute with each other, then: (i) two derivations of the form of the thermal state are invalid [6,8]; (ii) the Hamiltonian has degeneracies, which hinder arguments for thermalization [21]; and (iii) the eigenstate-thermalization hypothesis, one of the most

widely used explanations of quantum many-body thermalization internally, breaks down [38]. Hence the extent to which noncommuting charges permit thermalization is unclear.

We experimentally observe thermalization to near ρ_{NATS}, implementing the proposal in Ref. [21]. Our quantum simulator consists of 21 trapped ions. Two electronic states of each ion form a qubit. We initialize the qubits in an AMC subspace. The evolution—an effective long-range Heisenberg coupling—conserves the global-spin components $S_{x,y,z}^{\text{tot}}$. We implement the evolution by interspersing a long-range Ising coupling with global rotations and dynamical-decoupling sequences. Trotterization of Heisenberg dynamics has been proposed theoretically [50,51], realized experimentally in toy examples [52,53], and used very recently to explore many-body physics in ensembles of Rydberg atoms [54,55]; we demonstrate its effectiveness in many-body experiments on trapped ions. Two nearest-neighbor ions form the system of interest, the other ions forming an effective environment (Fig. 1). We measure the distance of $\mathcal{S}$ from ρ_{NATS}, finding significant thermalization on average over copies of $\mathcal{S}$ [6–9,45]. To begin to isolate the effects of the noncommutation on thermalization, we compare our experiment with an evolution that conserves just commuting charges: the Hamiltonian and S_z^{tot}. $\mathcal{S}$ remains farther from the thermal state if the charges fail to commute. This observation is consistent with the conjecture that noncommuting charges hinder thermalization [8], as well as with the expectation that, in finite-size global systems, resistance to thermalization grows with the number of charges [56,57]. Our experiment offers a particularly quantum counterpart to the landmark experiment [58] in which a hitherto-unobserved equilibrium state has been observed but the quantum physics of noncommutation of charges has been left unexplored. The present work opens up the emerging subfield of noncommuting thermodynamic charges to quantum many-body simulators.

II. EXPERIMENTAL SETUP

We begin by explaining the general experimental setup and protocol in Sec. II A. Section II B motivates and introduces our initial state.

A. Platform and protocol

We perform the experiment on a trapped-ion quantum simulator [59]. A linear string of $N = 21$ ^{40}Ca$^+$ ions is confined in a linear Paul trap [Fig. 1(a)]. The noncommutation of the charges is expected to influence many-body equilibration only in such mesoscale systems, as the correspondence principle dictates that systems grow classical as they grow large and that noncommutation of charges is nonclassical [8,21]. Let $S_\gamma = \sigma_\gamma/2$ (we set $\hbar = 1$), where σ_γ denotes the Pauli-γ operator, for $\gamma = x, y, z$.
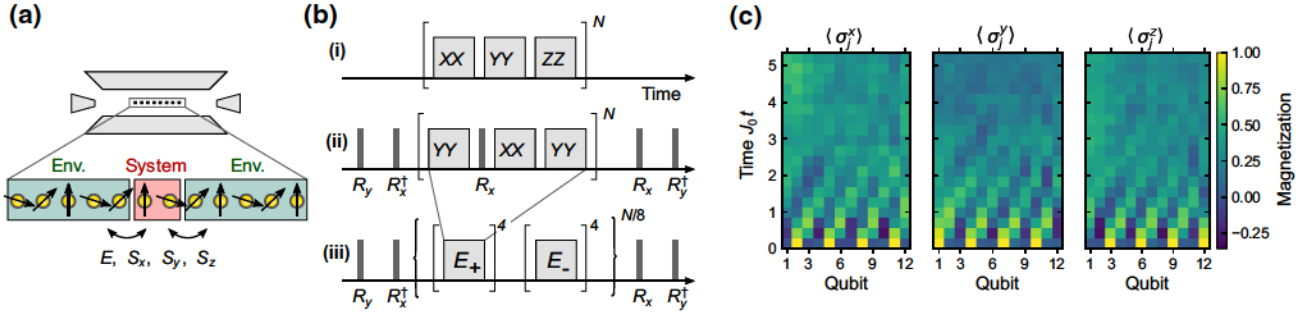
FIG. 1. The experimental setup and protocol. (a) A linear ion crystal of $N \leq 21$ qubits is trapped in a linear Paul trap. A small system exchanges charges (local instances of quantities that are conserved globally) with the surrounding environment: the energy, E, and all the components of angular momentum. (b) We Trotter approximate the Heisenberg evolution by evolving the state under each of the three terms of the Hamiltonian [Eq. (3)] consecutively, in short time steps. We experimentally realize two terms directly and generate the third term using resonant $\pi/2$ pulses (R_x and R_y). This pulse sequence further protects the state against dephasing noise (ii). The Trotter sequence contains building blocks $E_{\pm}$. Alternating between them reduces pulse-length errors (iii). For further details, see Appendix A. (c) The observed evolution of the 12-qubit initial state, $|y+, x+, z+\rangle^{\otimes 4}$, under the Trotter-approximated Heisenberg model (wherein $J_0 = 356$ rad/s and $\alpha = 0.70$). To characterize the dynamics fully, we derive the spin-excitation hopping rate in Appendix B.

Let $|\gamma \pm\rangle$ denote the ± 1 eigenstates of σ_γ. We denote by $\sigma_\gamma^{(j)}$ the site-j Pauli operators; and, by $\sigma_\gamma^{tot} = \sum_{j=1}^{N} \sigma_\gamma^{(j)}$, the whole-chain operators. Each ion encodes a qubit in the Zeeman states $3^2D_{5/2}$ and $4^2S_{1/2}$, of the respective magnetic quantum numbers $m = 5/2$ and $1/2$. We denote the states by $|z+\rangle$ and $|z-\rangle$. Two nearest-neighbor qubits form the small system of interest; the remaining qubits form the environment.

We employ two types of coherent operations using a laser at 729 nm, which drives the quadrupole transition that connects the qubit states. (i) Denoting a rotated Pauli operator by $\sigma_\phi^{(j)} = \cos\phi\, \sigma_x^{(j)} + \sin\phi\, \sigma_y^{(j)}$, we perform global qubit rotations $U(\theta, \phi) = \exp(-i\theta/2 \sum_{j=1}^{N} \sigma_\phi^{(j)})$. (ii) The effective long-range x-type Ising Hamiltonian,

$$H_{xx} := \sum_{j < k} \frac{J_0}{|j-k|^\alpha} \sigma_x^{(j)} \sigma_x^{(k)}, \quad (2)$$

entangles qubits [60]. We effect H_{xx} by off-resonantly coupling to the lower and upper vibrational sideband transitions of the transverse collective modes of the ion string [61]. Combining these two ingredients, we Trotter approximate the Heisenberg Hamiltonian,

$$H_{\text{Heis}} := \sum_{j < k} \frac{J_0}{3\,|j-k|^\alpha} \left(\sigma_x^{(j)} \sigma_x^{(k)} + \sigma_y^{(j)} \sigma_y^{(k)} + \sigma_z^{(j)} \sigma_z^{(k)} \right), \quad (3)$$

as shown in Fig. 1(b) and Appendix A. The 1/3 appears because the Ising coupling given in Eq. (2) is distributed across three directions (x, y, and z). We implement a $\sigma_y^{(j)} \sigma_y^{(k)}$ coupling similarly, as described in Appendix A. The pulse sequence is designed to realize H_{xx} while, via

dynamical decoupling, mitigating dephasing and rotation errors.

At the beginning of each experimental trial, the transverse collective modes of the ion string are cooled to near their motional ground state. Then, we prepare the qubits in the product state described in Sec. II B. We then evolve the global system for a time t up to $J_0 t_f = (357 \text{ rad/s}) \times (15 \text{ ms}) \approx 5.4$ [Fig. 1(c)]. The global system has largely equilibrated internally and fluctuations are small, as shown in Sec. III A. Finally, we measure the states of pairs of neighboring qubits via quantum state tomography. We measure the nontrivial expectation values of the two-qubit Pauli operators across many trials [21, Appendix G].

B. Initial state

Conventional thermalization experiments begin with the global system in a microcanonical subspace, a joint eigenspace shared by the global charges (apart from the energy). As our global charges do not commute, they cannot have well-defined nonzero values simultaneously; no nontrivial microcanonical subspace exists. We therefore prepare the global system in an AMC subspace, where the charges have fairly well-defined values. We follow the proposal in Ref. [21] for extending the definition of the AMC subspace, devised abstractly in Ref. [8], to realistic systems. In an AMC subspace, each global charge Q_γ^{tot} has a variance of approximately $O(N^\nu)$, wherein $\nu \leq 1$. Every tensor product of single-qubit pure states meets this requirement [21].

We choose the product to answer an open question. In Ref. [21], ρ_{NATS} has been found numerically to predict the long-time state of a small system best. However, other thermal states approached ρ_{NATS} in accuracy as N

grew. (The accuracy has been quantified with the relative-entropy distance of the long-time state to a thermal state, as detailed in Sec. III.) Does the accuracy of NATS remain greatest by an approximately constant amount, as N grows, for any initial state? The answer is yes for all N realized in our experiment.

The initial state,

$$|\psi_0\rangle := |y+, x+, z+\rangle^{\otimes N/3}, \tag{4}$$

consistently distinguishes the NATS for an intuitive reason synopsized here and detailed in Appendix C. The initial state determines the inverse temperature β and chemical potentials μ_γ in Eq. (1) [21] as follows. Denote the global NATS by $\rho_{\text{NATS}}^{\text{tot}} := \exp\left(-\beta\left[H_{\text{Heis}} - \sum_{\gamma=x,y,z}\mu_\gamma S_\gamma^{\text{tot}}\right]\right)/Z_{\text{NATS}}^{\text{tot}}$, wherein $Z_{\text{NATS}}^{\text{tot}}$ normalizes the state. β and the μ_γs are defined through [21,62]

$$\langle\psi_0|H_{\text{Heis}}|\psi_0\rangle = \text{Tr}\left(H_{\text{Heis}}\,\rho_{\text{NATS}}^{\text{tot}}\right) \tag{5}$$

and

$$\langle\psi_0|\sigma_\gamma^{\text{tot}}|\psi_0\rangle = \text{Tr}\left(\sigma_\gamma^{\text{tot}}\,\rho_{\text{NATS}}^{\text{tot}}\right) \quad \forall\gamma = x, y, z. \tag{6}$$

As the temperature approaches infinity, all thermal states converge to the maximally mixed state and so lose their distinguishability. We therefore choose the initial state such that β is finite. Additionally, the chemical potentials should be large, such that all noncommuting charges influence ρ_{NATS} substantially. Upon choosing $|\psi_0\rangle$, we calculate β and the μ values from Eq. (6) numerically, by solving a maximum-entropy problem, following Refs. [63,64]: $\beta = 1.3 \times 10^{-3}$ s/rad and $\mu_{x,y,z} = -1046$ rad/s.

For generality, we also test other initial states. Permuting the factors in Eq. (4), we change the temperature of the initial state. However, our qualitative conclusions continue to hold.

III. RESULTS

Having introduced our setup and protocol, we observe, in Sec. III A, the dynamics of thermalization influenced by noncommuting charges. Section III B evidences thermalization to near ρ_{NATS}. Section III C compares these results with thermalization in the presence of just two commuting charges.

A. Dynamics

Figure 2 shows how accurately the NATS predicts the state of a small system, as a function of time. The global system size is $N = 21$. To construct the blue dots, we measure the time-dependent state $\rho_t^{(j,j+1)}$ of each nearest-neighbor qubit pair $(j, j+1)$, for $j = 1, 2, \ldots, N-1$. We
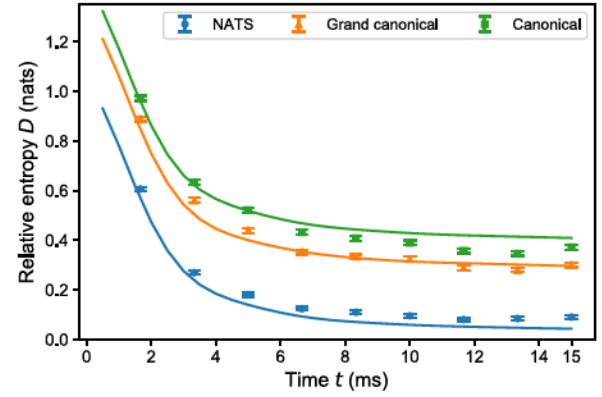

FIG. 2. The average distance from the system-of-interest state to the thermal prediction versus time. The ion chain consists of $N = 21$ qubits. Each nearest-neighbor pair forms a small system of interest. We measure the distance of the state to the NATS (blue points), using the relative entropy [8], and average over the pairs in the chain. The markers show experimental data, while the lines are calculated numerically from Eq. (3). Each data point is formed from 250 repetitions. The error bars are estimated by bootstrapping [66]. The entropies are measured in units of nats (are to base e). We also compare the NATS prediction with two competitor thermal predictions, following Refs. [21,47,58]: canonical and grand canonical states. At all times, the NATS predicts the state unambiguously more accurately than the competitors do.

then calculate the distance of the state to the NATS, measured with the relative entropy used often in quantum information theory [65]. If χ and ξ denote quantum states (density operators) defined on the same Hilbert space, the *relative entropy* is $D(\chi\|\xi) = \text{Tr}(\chi[\log\chi - \log\xi])$. (All logarithms in this paper are to base e: entropies are measured in units of nats—not to be confused with the NATS—rather than in bits.) The relative entropy boasts an operational interpretation: $D(\chi\|\xi)$ quantifies the optimal efficiency with which the states can be distinguished, on average, in a binary hypothesis test [65]. The relative entropy to the NATS has been bounded with quantum information-theoretic techniques [8] and calculated numerically in simulations [21]. Appendix D describes how we calculate ρ_{NATS} numerically. We average $D(\rho_t^{(j,j+1)}\|\rho_{\text{NATS}})$ over the $N-1$ qubit pairs, producing $\langle D(\rho_t^{(j,j+1)}\|\rho_{\text{NATS}})\rangle$. To our knowledge, this is the first report on the process of quantum many-body thermalization colored by noncommuting charges (e.g., begun in an AMC subspace).

As in Refs. [47,58], we compare the state of the small system with competing predictions by other thermal states: the canonical state $\rho_{\text{can}} := e^{-\beta H}/Z_{\text{can}}$ and the grand canonical state $\rho_{\text{GC}} := \exp\left(-\beta\{H - \mu_z S_z^{(2)}\}\right)/Z_{\text{GC}}$. The partition functions Z_{can} and Z_{GC} normalize the states. We denote by H the two-site Hamiltonian and by $S_z^{(2)}$ the two-site spin operator. We call ρ_{GC} "grand canonical" because S_z

is equivalent to a spinless-fermion particle-number operator via a Jordan-Wigner transformation [67]. As the blue disks (distances to ρ_{NATS}) are lower than the orange triangles (ρ_{GC}) and green squares (ρ_{can}), the NATS always predicts the state best.

The curves show results from numerical simulations. In the simulations, we exactly model time evolution under the Heisenberg Hamiltonian. The experimental markers lie close to the theoretical curves. Yet the distance to ρ_{GC} is slightly less empirically than theoretically, on average over time; the same is true of ρ_{can} and the opposite is true of ρ_{NATS}. These slight mismatches arise from noise, which we now describe.

As a real-world quantum system, the ion chain is open. The environment affects the chain similarly to a depolarizing channel, which brings the state toward the maximally mixed state, $\mathbb{1}/2^N$ [65]. Of our candidate two-qubit thermal states, ρ_{can} lies closest to $\mathbb{1}/4$, ρ_{GC} lies second closest, and ρ_{NATS} lies farthest. We can understand why information theoretically [7,9,45]. If one knows nothing about the system of interest, one can mostly reasonably ascribe to the system the state $\mathbb{1}/4$. Knowing nothing except the average energy, one should ascribe ρ_{can}. Knowing only the average energy and $\langle S_z^{(2)} \rangle$, one should ascribe ρ_{GC}. Knowing the average energy and $\langle S_{x,y,z}^{(2)} \rangle$, one should ascribe ρ_{NATS}. The more information a thermal state encodes, the farther it is from $\mathbb{1}/4$. The depolarizing noise, bringing the state of the two ions closer to $\mathbb{1}/4$, brings the state closer to ρ_{can} and ρ_{GC} but not so close to ρ_{NATS} (in fact, away from ρ_{NATS}, as explained in Appendix E): hence the deviations between experimental markers and theoretical predictions in Fig. 2.

Nonetheless, the experiment exhibits considerable resilience to noise. The chain can leak four charges ($S_{x,y,z}$ and energy) to its environment, violating the conservation laws ideally imposed on the ions. One might expect these many possible violations to prevent ρ_{NATS} from predicting the long-time state accurately. However, our results show otherwise: the chain is closed enough that ρ_{NATS}, as a prediction, bests all competitor thermal states that may be reasonably expected from thermodynamics and information theory [45]. Appendix E supports this conclusion with simulations of depolarization atop the Trotterized Heisenberg evolution.

By $t_f = 15$ ms, the curves in Fig. 2 are approximately constant; the small system has approximately thermalized. Thermalization occurs more completely at large N than at small N but 15 ms suffices for all the curves to drop substantially. Our choice of experimental run time is thereby justified (for details about fluctuations in the relative entropy, see Appendix G).

B. Thermalization to near the non-Abelian thermal state

In Fig. 3, we focus on late times while varying the global system size. We average over the final three time points,

as the relative entropies have equilibrated but fluctuate slightly across that time (Appendix G). The blue disks represent the relative-entropy distance from the final system-of-interest state, $\rho_{t_f}^{(j,j+1)}$, to the NATS, averaged over qubit pairs. The average distance declines from 0.24(2) nats to 0.085(6) nats as N grows from 6 to 21. These values overestimate the true values by approximately 0.03 nats, because the number of experimental trials is finite. For reference, $D(\chi||\xi)$ obeys no upper bound. We hence answer two open questions. Equilibration to near the NATS occurs in realistic systems and is experimentally observable, despite the opportunity for the spin chain to leak many charges via decoherence. Furthermore, the orange triangles (distances to ρ_{GC}) lie 0.16 nats above the blue disks (distances to ρ_{NATS}), on average; and the green squares (distances to ρ_{can}) lie 0.26 nats above the blue disks, on average. Hence the NATS prediction is distinguishably most accurate at all experimentally realized N.

Appendix F analytically extends this conclusion beyond the experimental system sizes. Consider averaging each thermal state over the qubit pairs. The averaged ρ_{NATS} differs from the averaged competitor thermal states, as measured by nonzero relative-entropy distances. The distances are lower bounded by a constant at all N, even in the thermodynamic limit (as $N \to \infty$). We prove this claim about the distinguishability of ρ_{NATS} under the assumptions met by our experiment.

We observe equilibration to near the NATS but the small system does not thermalize entirely: $\langle D(\rho_{t_f}^{(j,j+1)}||\rho_{NATS}) \rangle \neq 0$. We expect the lingering athermality to stem partially from the finite size of the global system [68,69]. Yet noncommutation of charges has been conjectured to hinder
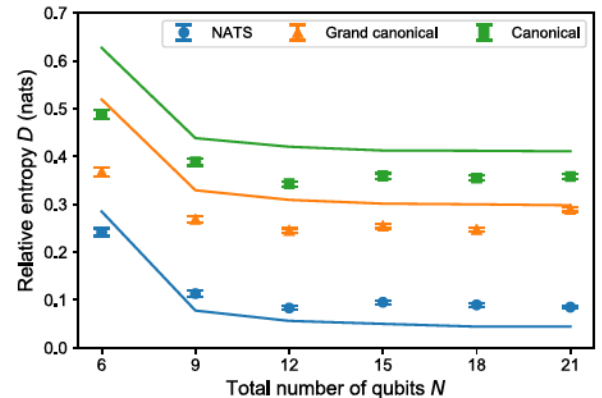

FIG. 3. The average distance from the long-time system-of-interest state to the thermal prediction versus total number of qubits. The markers show experimental data, while the lines are calculated numerically, using unitary dynamics, from Eq. (3). The NATS predicts the final state the most accurately at all system sizes. Depolarizing noise appears to explain the experiment-theory discrepancies. The $N = 6$ point is an outlier due to the small size of the global system.

FLORIAN KRANZL <i>et al.</i>

PRX QUANTUM 4, 020318 (2023)

TABLE I.   The average distance from the long-time system-of-interest state to the grand canonical state, ρ_{GC}, when only energy and σ_z^{tot} are conserved. Each nearest-neighbor pair in the ion chain forms a small system of interest. The long-time state of the pair lies some distance from ρ_{GC} (the most accurate thermal prediction). We measure this distance using the relative entropy D [8], measured in nats. Then, we average over the pairs in the chain. The average pair thermalizes more thoroughly than if noncommuting charges are conserved, at all global system sizes N.

N	6	9	12	15	18	21
D	0.19(2)	0.096(10)	0.077(6)	0.066(7)	0.057(5)	0.056(6)

thermalization additionally [21]. We now dig further into that conjecture.

C. Comparison with commuting charges

Let us compare thermalization steered by noncommuting charges with thermalization steered by just commuting charges. We realize the commuting case with the long-range <i>XY</i> Hamiltonian

$$H_{xy} := \sum_{j<k} \frac{1}{2} \frac{J_0}{|j-k|^\alpha} \left(\sigma_x^{(j)}\sigma_x^{(k)} + \sigma_y^{(j)}\sigma_y^{(k)} \right), \quad (7)$$

for $N = 21$, with $J_0 = 398$ rad/s and $\alpha = 0.86$ (for details, see Appendix A). The charges are the total energy and σ_z^{tot}. We Trotter approximate H_{xy} similarly to H_{Heis} (Appendix H). We prepare $|y+, x+, z+\rangle^{\otimes N/3}$, such that the commuting-charge experiment parallels the noncommuting-charge experiment (which begins in an AMC subspace too) as closely as possible. Then, we simulate H_{xy} for 10 ms [70].

Table I shows the results. The average small system thermalizes more thoroughly when determined by commuting charges than when determined by noncommuting charges. For instance, in the commuting case, the relative entropy to ρ_{GC} descends as low as 0.056(6) nats, when $N = 21$. In the noncommuting case, when $N = 21$, the relative entropy to ρ_{NATS} reaches $0.085(6) > 0.056(6)$ nats. This result is consistent with the conjecture that noncommutation of charges hinders thermalization [21], as well as with the expectation that, in finite-size global systems, the long-time entanglement entropy of a small system decreases as the number of charges grows [57]. Future work will distinguish how much the noncommutation of our charges is hindering thermalization and how much the multiplicity of charges is.

IV. CONCLUSIONS

We observe the first experimental evidence of a particularly quantum equilibrium state, the non-Abelian thermal state, which depends on noncommuting charges. Whereas typical many-body experiments begin in a microcanonical subspace, our experiment begins in an approximate microcanonical subspace. This generalization accommodates the inability of the noncommuting charges to have well-defined nontrivial values simultaneously. Our experiment provides an affirmative answer to an open question: whether, for any initial state, the NATS remains a substantially better prediction than other thermal states as the global system grows. Our trapped-ion experiment affirmatively answers two more open questions: (i) whether realistic systems exhibit the thermodynamics of noncommuting charges; and (ii) whether this thermodynamics can be observed experimentally, despite the abundance of the conservation laws that decoherence can break. Our work therefore bridges quantum simulators to the emerging subfield of noncommuting charges in quantum information thermodynamics. The subfield has remained theoretical until now; hence many predictions now can, and should, be tested experimentally—predictions about reference frames, second laws of thermodynamics, information storage in dynamical fixed points, and more [5–39].

In addition to answering open questions, our results open up avenues for future work. First, Fig. 3 contains blue disks (distances to ρ_{NATS}) that could be fitted. The best-fit line could be compared with the numerical prediction in Ref. [8] and the information-theoretic bound in Ref. [21]. Obtaining a reliable fit would require the reduction of systematic errors, such as decoherence, and the performance of more trials. Second, we observe that the small system thermalizes less in the presence of noncommuting charges than in the presence of just commuting charges. Future studies will tease apart the effects of the noncommutation of charges from those of the multiplicity of charges.

Third, the quantum simulation toolkit developed here merits application to other experiments. We combine the native interaction of our quantum simulator with rotations and dynamical decoupling to simulate a non-native Heisenberg interaction. The Trotterized long-range Hamiltonian, with the single-qubit control used to initialize our system, can be advantageous for studying more many-body physics with quantum simulators. As our experiment reaches system sizes larger than can reasonably be simulated realistically (including noise), the usefulness of our toolkit in many-body physics is evident. These techniques can be leveraged to explore nonequilibrium Heisenberg dynamics [54,55], topological excitations [71], and more. Beyond the Heisenberg model, the impact of noncommutation of charges on equilibration can be studied in more exotic contexts, such as lattice gauge theories [4,72].

ACKNOWLEDGMENTS

N.Y.H. thanks Michael Beverland, Ignacio Cirac, Markus Greiner, Julian Léonard, Mikhail Lukin, Vladan Vuletic, and Peter Zoller for insightful conversations.

020318-6

APPENDIX A: METHODS

This appendix provides details about the setup (Sec. A 1), the realization of spin-spin interactions (Sec. A 2), the Trotterization of the Heisenberg Hamiltonian (Sec. A 3), and the quantum state tomography and statistical analysis (Sec. A 4).

1. Experimental setup

A linear ion crystal of 21 ^{40}Ca$^+$ ions is trapped in a linear Paul trap with trapping frequencies of $\omega_x = 2\pi \times 2.930$ MHz (radially) and $\omega_{ax} = 2\pi \times 0.217$ MHz (axially). The qubit states $|z+\rangle$ and $|z-\rangle$ are coupled by an optical quadrupole transition, which we drive with a titanium-sapphire laser, with a sub-10-Hz line width, at 729 nm. Collective qubit operations are implemented with a resonant beam that couples to all the qubits with approximately equal strengths. Single-qubit operations are performed with a steerable tightly focused beam that induces ac Stark shifts. In some trials, the system size N is less than 21. In these cases, we hide the unused ions in the Zeeman sublevel $|3^2D_{5/2}, m = -3/2\rangle$.

Recall that the initial state is ideally the product $|\psi_0\rangle$ in Eq. (4). The experimental initial state $|\psi_{exp}\rangle$ has a fidelity $|\langle\psi_{exp}|\psi_0\rangle|^2 = 0.90(2)$ for $N = 21$. In each experimental cycle, we cool the ions via Doppler cooling and polarization-gradient cooling [73]. We also sideband cool all transverse collective motional modes to near their ground states. Then, we prepare the state equation [see Eq. (4)], simulate the Heisenberg evolution, and measure the state. The cycle is repeated 300–500 times per quantum state-tomography measurement basis.

2. Implementing the effective Heisenberg interaction

We implement the long-range spin-spin interaction given in Eq. (2) with a laser beam carrying two frequencies that couple the motional and electronic degrees of freedom of the ion chain. The frequency components of the beam, $\omega_\pm = \pm(\omega_x + \Delta)$, are symmetrically detuned by $\Delta = 2\pi \times 27$ kHz (for $N = 21$ ions) from the transverse-center-of-mass mode, which has a frequency $\omega_x = 2\pi \times 2.930$ MHz. A third frequency component, $\omega_{ac} = 2\pi \times 1.4$ MHz, is added to the bichromat beam. This component compensates for the additional ac Stark shift caused by other electronic states [74].

The resulting spin-spin coupling effects a long-range Ising model, $\sum_{j<k} J_{j,k}\sigma_x^{(j)}\sigma_x^{(k)}$. The $J_{j,k}$ denotes the strength of the coupling between ions j and k. $J_{j,k}$ approximates the power law in Eq. (2), where the coupling strength equals $J_0 = 468$ s/rad and the exponent $\alpha = 0.86$ for the 21-ion chain.

Direct realization of the desired long-range Heisenberg Hamiltonian in Eq. (3) for trapped ions is difficult [61,75]. Instead, we simulate H_{Heis} via Trotterization. After the first time step, we change the interaction from H_{xx} to H_{yy}; after the second time step, to H_{zz}; and, after the third time step, back to H_{xx}. We perform this cycle, or *Trotter step*, N_T times [76]. We can realize H_{yy} by shifting the phase of the bichromat light by $\pi/2$ relative to the phase used to realize H_{xx}. The implementation of H_{zz} requires a global rotation. Denote by R_y a $\pi/2$ rotation of all the qubits about the y axis. We can effect H_{zz} with, e.g., $R_y^\dagger H_{xx} R_y$.

3. Noise-robust Trotter sequence

In our experimental setup, most native decoherence is dephasing relative to the σ_z eigenbasis, which rotations transform into effective depolarization (Appendix E). This noise results from temporal fluctuations of (i) the magnetic field and (ii) the frequency of the laser that drives the qubits. Earlier experiments on this platform have involved XY interactions, which enable the quantum state to stay in a decoherence-free subspace [74,77,78]. Here, the dynamics must be shielded from dephasing differently. We mitigate magnetic field noise by incorporating a dynamical-decoupling scheme into the Trotter sequence [Fig. 1(b)]. Furthermore, we design the Trotter sequence to minimize the number of global rotations. This minimization suppresses the error accumulated across all the rotations. We reduce this error further by alternating the directions of the rotations between Trotter steps (for further details, see Appendix H).

To formalize the Trotter sequence, we introduce the following notation. Let $U_{xx} = \exp(-iH_{xx}t)$ and $U_{yy} = \exp(-iH_{yy}t)$. For $\gamma \in \{x, y\}$, $R_\gamma := \exp(-i\pi/4\,\sigma_\gamma^{tot})$ denotes a global $\pi/2$ rotation about the γ axis. N_T denotes the number of Trotter steps. Each Trotter step consists of either the operation $E_+ = U_{yy}U_{xx}R_xU_{yy}$ or the operation

$E_- = U_{yy} U_{xx} R_x^\dagger U_{yy}$. To simulate a Heisenberg evolution for a time t, we implement the Trotter sequence

$$U_{\text{Heis}}(t) \approx R_y^\dagger R_x \left[(E_-)^4 (E_+)^4 \right]^{N_T/8} R_x^\dagger R_y. \quad \text{(A1)}$$

This sequence protects against decoherence and over- or under-rotation errors caused by global pulses. Numerical simulations supporting this claim appear in Appendix I.

The Trotter sequence lasts for 15 ms, containing ≤ 36 Trotter steps. Each Trotter step consists of three substeps, each lasting for approximately 139 μs. The rising and falling slopes of each substep are pulse shaped to avoid incoherent excitations of vibrational sidebands of the qubit transition. The slopes reduce the effective spin-spin coupling by a factor of 0.84 and the actual interaction time is 115 μs. Thus, the effective spin-spin coupling values used in Eq. (3) range from $J_0 = 336$ rad/s for six qubits to $J_0 = 398$ rad/s for 21 qubits.

The magnetic field variations occur predominantly at temporally stable 50-Hz harmonics. We reduce the resulting Zeeman-level shifts via feed-forward to a field-compensation coil [59]. The amplitudes end up below 3 Hz, for all 50-Hz harmonics between 50 Hz and 900 Hz. Consider a simple Ramsey experiment on the qubit transition $4^2S_{1/2}(m = +1/2) \leftrightarrow 3^2D_{5/2}(m = +5/2)$. The corresponding $(1/e)$-contrast coherence time is 47(6) ms. The global qubit rotations are driven by the elliptically shaped 729-nm beam, which causes spatially inhomogeneous Rabi frequencies that vary across the ion crystal by 6%.

4. Quantum state tomography

We measure the state of each qubit pair via quantum state tomography. In each measurement basis, 300–500 quantum state measurements are carried out. To reconstruct the state from the measurements, we use maximum-likelihood estimation [79]. We estimate statistical uncertainties by bootstrapping [66].

APPENDIX B: RATE OF HOPPING DURING HEISENBERG EVOLUTION

In this appendix, we derive an expression for the spin-exchange rate of the Heisenberg Hamiltonian. For simplicity, we model two qubits governed by the Heisenberg Hamiltonian

$$H = \frac{J_0}{3} \left(\sigma_x^{(1)} \sigma_x^{(2)} + \sigma_y^{(1)} \sigma_y^{(2)} + \sigma_z^{(1)} \sigma_z^{(2)} \right). \quad \text{(B1)}$$

We relabel the σ_z eigenstates as $|z+\rangle \equiv |\uparrow\rangle$ and $|z-\rangle \equiv |\downarrow\rangle$. Matrices are expressed relative to the basis formed from products of $|\uparrow\rangle$ and $|\downarrow\rangle$. The Hamiltonian can be expressed as

$$H = \frac{J_0}{3} \begin{pmatrix} 1 & 0 & 0 & 0 \\ 0 & -1 & 2 & 0 \\ 0 & 2 & -1 & 0 \\ 0 & 0 & 0 & 1 \end{pmatrix}, \quad \text{(B2)}$$

and a pure two-qubit state as $|\psi(t)\rangle = c_1(t)|\downarrow\downarrow\rangle + c_2(t)|\uparrow\downarrow\rangle + c_3(t)|\downarrow\uparrow\rangle + c_4(t)|\uparrow\uparrow\rangle$. The coefficients $c_k(t) \in \mathbb{C}$ depend on the time, t, and are normalized as $\sum_{k=1}^{4} |c_k(t)|^2 = 1$. The dynamics obey the Schrödinger equation, $H|\psi(t)\rangle = i\hbar d|\psi(t)\rangle/dt$. Defining $\Omega := J_0/3$ and setting $\hbar = 1$, we express the Schrödinger equation in matrix form as

$$\begin{pmatrix} \dot{c}_1(t) \\ \dot{c}_2(t) \\ \dot{c}_3(t) \\ \dot{c}_4(t) \end{pmatrix} = -i\Omega \begin{pmatrix} 1 & 0 & 0 & 0 \\ 0 & -1 & 2 & 0 \\ 0 & 2 & -1 & 0 \\ 0 & 0 & 0 & 1 \end{pmatrix} \begin{pmatrix} c_1(t) \\ c_2(t) \\ c_3(t) \\ c_4(t) \end{pmatrix}. \quad \text{(B3)}$$

The solution is

$$c_1(t) = c_1(0)e^{-i\Omega t},$$

$$c_2(t) = \frac{1}{2}c_2(0)e^{-i\Omega t}(1 + e^{4i\Omega t}) + \frac{1}{2}c_3(0)e^{-i\Omega t}(1 - e^{4i\Omega t}),$$

$$c_3(t) = \frac{1}{2}c_3(0)e^{-i\Omega t}(1 + e^{4i\Omega t}) + \frac{1}{2}c_2(0)e^{-i\Omega t}(1 - e^{4i\Omega t}),$$

$$c_4(t) = c_4(0)e^{-i\Omega t}. \quad \text{(B4)}$$

We aim to derive the time required for $|\uparrow\downarrow\rangle$ to transform into $|\downarrow\uparrow\rangle$. If the initial state is $|\psi(0)\rangle = |\uparrow\downarrow\rangle$, the solution reduces to

$$c_1(t) = 0,$$

$$c_2(t) = \frac{1}{2}e^{-i\Omega t}(1 + e^{4i\Omega t}),$$

$$c_3(t) = \frac{1}{2}e^{-i\Omega t}(1 - e^{4i\Omega t}),$$

$$c_4(t) = 0.$$

Consider measuring the σ_z product eigenbasis at time t. The possible outcomes $\uparrow\downarrow$ and $\downarrow\uparrow$ result with probabilities

$$|c_2(t)|^2 = \frac{1}{4}(2 + e^{4i\Omega t} + e^{-4i\Omega t}) = \frac{1}{2} + \frac{1}{2}\cos(4\Omega t) \quad \text{(B5)}$$

and

$$|c_3(t)|^2 = 1 - |c_2(t)|^2. \quad \text{(B6)}$$

Therefore, the two-qubit excitation-hopping frequency is $\Gamma_{\text{flip-flop}} = 4\Omega = 4J_0/3$. The corresponding period is

defined as the hopping time:

$$T_{\text{hop}} = \frac{2\pi}{2\Gamma_{\text{flip-flop}}} = \frac{3\pi}{4J_0}. \tag{B7}$$

This result agrees with our experimental results and can be extended simply to N qubits. If the interaction is nearest-neighbor only, the time for hopping from site 1 to site N is $T_{\text{hop}} = (N-1)3\pi/4J_0$.

APPENDIX C: INITIAL STATE

If the global system is prepared in $|\psi_0\rangle$ [Eq. (4)], ρ_{NATS} models the long-time state of a small system distinctly more accurately than other thermal states (ρ_{can} and ρ_{GC}) do, at all the global system sizes N realized (Fig. 3). Equation (4) distinguishes ρ_{NATS} for two reasons.

First, suppose that the temperature is high ($\beta \gtrsim 0$). All the thermal states resemble the maximally mixed (infinite-temperature) state $\mathbb{1}/2^N$ and so resemble each other. We therefore keep the temperature low, by keeping the spatial density of each charge low. We separate the $|\gamma+\rangle$s from each other maximally, for each $\gamma = x, y, z$. To provide a sense of the size of β at $N = 12$, we compare with the bandwidth of the Heisenberg Hamiltonian given in Eq. (3), the greatest energy minus the least. β equals 7.13 times the inverse of the bandwidth and 1.74×10^{-3} times the inverse of the average energy gap.

Second, noncommuting charges distinguish NATS thermodynamics from more classical thermodynamics. If we are to observe NATS physics, therefore, ρ_{NATS} [Eq. (1)] should depend significantly on Q_γ^{tot}, for all γ. Hence the μ_γs should have large magnitudes—and so should the expectation values $\langle\psi_0|\sigma_\gamma^{\text{tot}}|\psi_0\rangle$, by Eq. (6). Hence, for each γ, the σ_γ eigenstates in $|\psi_0\rangle$ should be identical. The ordering of the $x+$, $y+$, and $z+$ in Eq. (4) does not matter. Importantly, $|\psi_0\rangle$ is not an eigenstate of any Q_γ^{tot}, so the global system does not begin in a microcanonical subspace; hence the experiment is not equivalent, by any global rotation, to any experiment that conserves just σ_z^{tot} and that leads to ρ_{GC}. When $N = 12$, $\beta\mu_z$ equals -1.36 times the inverse of each nonzero gap of S_z^{tot}.

We numerically identify many tensor products of the $|\gamma\pm\rangle$s, as well as superpositions of energy eigenstates, that have β values much greater than our β. These states suffer from drawbacks that render the states unsuitable for observing the NATS: either $\mu_{x,y,z} = 0$ or only one of the three charges has a nonzero expectation value. Such states provide little direction information about noncommutating charges. Furthermore, the states are highly entangled and so are difficult to prepare experimentally. $|\psi_0\rangle$ is easy to generate, aside from having a large $\sum_\gamma \beta\mu_\gamma S_\gamma^{\text{tot}}$.

APPENDIX D: NUMERICAL CALCULATION OF THE NON-ABELIAN THERMAL STATE

Consider calculating the NATS for qubits j and $j + 1$. One might substitute two-qubit observables into Eq. (1). This substituting yields an accurate prediction in the weak-coupling limit [21] However, the long-range interactions of the experiment render a many-body-physics approach more accurate [62]. We calculate β and $\mu_{x,y,z}$ from the definitions given in Eqs. (5) and (6), which depend on whole-system observables. Then, we construct the whole-system NATS in those equations, $\rho_{\text{NATS}}^{\text{tot}} :=$ $\exp\left(-\beta\left[H_{\text{Heis}} - \sum_{\gamma=x,y,z} \mu_\gamma S_\gamma^{\text{tot}}\right]\right)/Z_{\text{NATS}}^{\text{tot}}$. Finally, we trace out all the qubits except for j and $j + 1$.

We perform the trace stochastically [80], for computational feasibility. The stochastic trace requires an average over states selected Haar randomly from the traced-out subspace. We average over 50–1000 samples, the precise number determined for each N as follows. First, for small N, we calculate the trace exactly. We then determine the number of samples required for our stochastic approximation to converge to the exact value. From this number of samples, we estimate the number required for greater N. (To estimate, we scale down the sample size approximately inversely proportionally with the dimensionality of the traced-out Hilbert space, erring on the side of using more samples than necessary.) We sample this many Haar-random states and approximate the trace stochastically. Then, we slightly increase the number of samples, approximate the trace stochastically again, and confirm that the result does not change significantly.

APPENDIX E: EFFECT OF DEPOLARIZING NOISE ON RELATIVE ENTROPY

We expect depolarization to dominate the noise of our experiment. The reason is the experimental Hamiltonian and Trotter sequence, described in Appendix H 3, as well as the dominant native decoherence. We rotate the qubits to effectively transform the native $\sigma_x\sigma_x$ coupling into the Heisenberg Hamiltonian, which is isotropic. Meanwhile, dephasing relative to the σ_z eigenbasis dominates the native decoherence. The rotations spread the dephasing errors to the x, y, and z directions uniformly. Such isotropic errors effect depolarization [65]. This appendix reports on numerical simulations of depolarized Trotter evolutions. We infer that noise should not significantly affect the conclusions drawn from our experimental observations.

We simulate the Trotterized Heisenberg-Hamiltonian evolution, with and without depolarization, of 12 qubits. Depolarization probabilistically interchanges the 12-qubit state ρ with the maximally mixed state: $\rho \mapsto \mathcal{E}(\rho) = (1 - p)\rho + p\mathbb{1}/4$. We choose a noise parameter $p = 0.06$ and we apply the channel $\mathcal{E}$ every 1.5 ms. This p value is 30
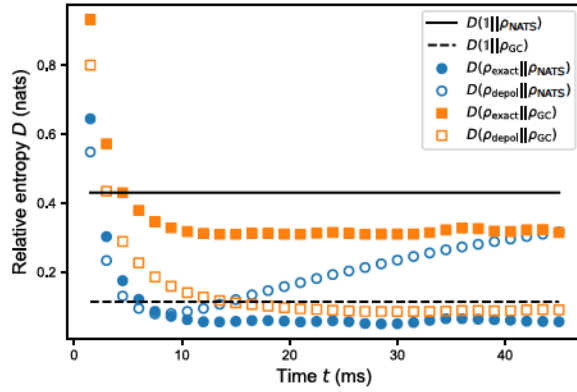
FIG. 4.   Relative entropies from simulations with and without depolarizing noise versus time. We simulate 12 qubits subject to Trotterized Heisenberg evolution alone (filled markers) or with depolarization (empty markers). The blue circles show relative-entropy distances to the NATS and the orange squares show distances to the grand canonical state.

times higher than the value that best reproduces the distance of the experimental state from ρ_{GC}. We simulate an evolution of 45 ms.

Figure 4 depicts the results of the simulation. Time runs along the x axis. Along the y axis is the relative entropy between a system-of-interest state and a thermal state, averaged over all the nearest-neighbor qubit pairs of the chain (Sec. III A). ρ_{exact} denotes the final state of the depolarization-free simulation and ρ_{depol} denotes the final state of the noisy simulation. We refer to the two states collectively as ρ. We plot the distance of each state to the NATS and distance to the grand canonical state. We omit ρ_{can} for conciseness, although we analyze this state too. All qualitative conclusions about ρ_{GC} apply to ρ_{can}. The simulation is intended to reproduce qualitative effects, rather than exact experimental numbers, as we lack independent quantitative evaluations of the experimental noise.

First, depolarizing noise affects $D(\rho||\rho_{\text{NATS}})$ oppositely to $D(\rho||\rho_{GC})$. The reason is that depolarization transforms the simulated state into the maximally mixed state. ρ_{GC} lies close to $\mathbb{1}/4$, closer than ρ_{exact} lies to ρ_{GC}. In Fig. 4, the dashed black line lies below the solid square markers at most times (Sec. III A explains why). Therefore, pushing ρ toward $\mathbb{1}/4$, depolarization pushes ρ farther toward ρ_{GC} (nudges the empty square markers downward from the solid square markers, toward the dashed black line). In contrast, ρ_{NATS} lies farther from $\mathbb{1}/4$ than ρ_{exact} lies from ρ_{NATS}: the solid black line lies above the filled disks at most times (again, Sec. III A explains why). Therefore, pushing ρ toward $\mathbb{1}/4$, depolarization pushes ρ farther from ρ_{NATS} (nudges the empty circles upward from the filled disks, toward the solid black line). Hence depolarization increases $D(\rho||\rho_{\text{NATS}})$ while decreasing $D(\rho||\rho_{GC})$.

Second, depolarization appears to affect $D(\rho||\rho_{\text{NATS}})$ more slowly than it affects $D(\rho||\rho_{GC})$. The reason is

that depolarization pushes $D(\rho||\rho_{GC})$ in the same direction as the Trotterized Heisenberg evolution—downward. Therefore, $D(\rho||\rho_{GC})$ decreases quickly. In contrast, depolarization competes with the Heisenberg evolution in pushing $D(\rho||\rho_{\text{NATS}})$ downward. This competition makes $D(\rho_{\text{depol}}||\rho_{\text{NATS}})$ depart from $D(\rho_{\text{exact}}||\rho_{\text{NATS}})$ slowly; the unfilled circles in Fig. 4 separate from the filled disks more slowly than the unfilled square markers separate from the filled square markers.

Third, although depolarization ultimately raises $D(\rho_{\text{depol}}||\rho_{\text{NATS}})$ well above $D(\rho_{\text{exact}}||\rho_{\text{NATS}})$ in our simulation, no such dramatic raising is visible in the experimental plot Fig. 2. That is, the empty circles in Fig. 4 rise well above the filled disks; yet the blue disks in Fig. 2 scarcely rise at the end of the experiment. Therefore, the experimental noise is weak and does not substantially affect $\langle D(\rho_t^{(j,j+1)}||\rho_{\text{NATS}})\rangle$.

Overall, the noise simulation affirms our main conclusion. We expect the experimental noise not to affect $D(\rho||\rho_{\text{NATS}})$ significantly while lowering $D(\rho||\rho_{GC})$ somewhat. Regardless of noise, the simulated state $\rho_{\text{exact/depol}}$ lies closest to ρ_{NATS} by a large margin. We can therefore have confidence that the predictive accuracy of NATS does not stem from the dominant noise.

Simulation of the XY model yields different results but the same conclusion: noise affects the experimental results insignificantly. The XY model conserves only two charges (σ_z^{tot} and the Hamiltonian), so ρ_{NATS} should not predict the long-time state accurately. Indeed, $D(\rho||\rho_{\text{NATS}}) > D(\rho||\rho_{GC})$ at long times; and depolarization increases both relative entropies. Due to this parallel increase, and because the experimental noise appears to be weak, noise is again not expected to affect our conclusion: regardless of noise, ρ_{GC} should predict the long-time state best under the evolution of the XY model.

APPENDIX F: DISTINCTION BETWEEN NON-ABELIAN THERMAL STATE AND COMPETITORS AT ALL GLOBAL SYSTEM SIZES

The main text answers a question established in Ref. [21]. Consider a global system of N subsystems, which exchange noncommuting charges. Consider measuring the long-time state of one subsystem. Measure the distance of the state to ρ_{NATS} and to the competitor thermal states: the canonical ρ_{can} and the grand canonical ρ_{GC}. The NATS has been found numerically, in Ref. [21], to predict the final state most accurately. However, as N grow, ρ_{can} and ρ_{GC} approaches ρ_{NATS} in accuracy. The reason is believed to be the initial global state, which has a high temperature and low chemical potentials (see Appendix A). Does ρ_{NATS} remain substantially more accurate at all N, for any initial state $|\psi_0\rangle$? Or do all the thermal-state predictions converge in the thermodynamic limit (as $N \to \infty$), for every $|\psi_0\rangle$?

Our experiment suggests the former, as explained in Sec. III. We construct a $|\psi_0\rangle$ for which the NATS prediction remains more accurate than the ρ_{can} and ρ_{GC} predictions, by approximately constant-in-N amounts, at all N values realized experimentally (Fig. 3). Appendix A provides one perspective on why this $|\psi_0\rangle$ distinguishes the thermal states. We provide another perspective here.

We prove that, under conditions realized in our experiment, ρ_{NATS}, averaged over space, differs from the average ρ_{can} and ρ_{GC}. This difference remains nonzero even in the thermodynamic limit. Appendix F 1 presents the setup, which generalizes our experiment's setup. In Appendix F 2, we formalize and prove the result [81]. Appendix F 3 shows how our experiment realizes the general setup.

1. Setup

Consider a global system of N identical subsystems. Let $O^{(j)}$ denote observable O of subsystem j. Sometimes, $O^{(j)}$ will implicitly be padded with identity operators $\mathbb{1}$ acting on the other subsystems. The corresponding global observable is $O^{tot} := \sum_{j=1}^{N} O^{(j)}$.

The Hamiltonian H^{tot} is translationally invariant. H^{tot} conserves global charges $Q_{\gamma}^{tot} := \sum_{j=1}^{N} Q_{\gamma}^{(j)}$, for $\gamma = 0, 1, 2, \ldots, c$. The charges do not all commute pairwise: $[Q_{\gamma}^{(j)}, Q_{\gamma'}^{(j)}] \neq 0$ for at least one pair (γ, γ').

We assume that some global unitary V satisfies two requirements. First, the unitary commutes with the Hamiltonian: $[V, H^{tot}] = 0$. Second, conjugating at least one global charge Q_{γ}^{tot} with V negates the charge:

$$V Q_{\gamma}^{tot} V^{\dagger} = -Q_{\gamma}^{tot}. \tag{F1}$$

We assume that the initial expectation value of this global charge is proportional to the global system size, as in the trapped-ion experiment:

$$\langle Q_{\gamma}^{tot} \rangle_0 = q_{\gamma} N \neq 0, \tag{F2}$$

for some constant-in-N q_{γ}.

Let $|\psi_0\rangle$ denote the initial global state. It is invariant, we assume, under translations through τ sites, for some non-negative integer τ. More precisely, divide the chain into clumps of τ subsystems. Index the clumps with $m = 1, 2, \ldots, N/\tau$. (We assume for convenience that N is an integer multiple of τ.) Consider tracing out all the subsystems except the mth clump: $\mathrm{Tr}_{1, 2, \ldots, (m-1)\tau, \, m\tau+1, m\tau+2, \ldots, N}(|\psi_0\rangle\langle\psi_0|)$. The form of this state does not depend on m.

Let us define a state averaged over clumps of subsystems. Let ρ denote any state of the global system. Consider the clump that, starting at subsystem j, encompasses τ

subsystems. This clump occupies the state

$$\rho^{(j, j+1, \ldots, j+\tau-1)} := \mathrm{Tr}_{1, 2, \ldots, j-1, \, j+\tau, j+\tau+1, \ldots, N}(\rho). \tag{F3}$$

Let $\mathcal{T}_j$ denote the operator that translates a state $j - 1$ sites leftward. We define the average

$$\rho^{avg} := \frac{1}{N} \sum_{j=1}^{N} \mathcal{T}_j \left(\rho^{(j, j\oplus 1, \ldots, j\oplus\tau\ominus 1)} \right) \tag{F4}$$

on the joint Hilbert space of subsystems 1 through τ. Addition and subtraction modulo N are denoted by $\oplus$ and $\ominus$. If ρ is fully translationally invariant (if $\tau = 1$), then $\rho^{avg} = \mathrm{Tr}_{2,3,\ldots,N}(\rho)$, and this definitional step can be skipped. Multiple thermal states will interest us. The global canonical state is defined as $\rho_{can}^{tot} := \exp(-\beta H^{tot})/Z_{can}^{tot}$. The partition function is $Z_{can}^{tot} := \mathrm{Tr}(e^{-\beta H^{tot}})$. The inverse temperature β is defined through $\langle\psi_0|H^{tot}|\psi_0\rangle = \mathrm{Tr}(H^{tot}\rho_{can}^{tot})$. Define the single-site $\rho_{can}^{(j)} := \mathrm{Tr}_{\bar{j}}(\rho_{can}^{tot})$. Denote by ρ_{can}^{avg} the result of averaging ρ_{can}^{tot} over clumps, as in Eq. (F4).

The global NATS is defined as

$$\rho_{NATS}^{tot} := \exp\left(-\beta\left[H^{tot} - \sum_{\gamma=1}^{c} \mu_{\gamma} Q_{\gamma}^{tot}\right]\right)/Z_{NATS}^{tot}. \tag{F5}$$

This β is defined analogously to the canonical β. The values of the temperatures values might differ but we reuse the symbol β for convenience. The effective chemical potentials μ_{γ} are defined through [21]

$$q_{\gamma} N = \mathrm{Tr}\left(Q_{\gamma}^{tot} \rho_{NATS}^{tot}\right). \tag{F6}$$

The partition function $Z_{NATS}^{tot} := \mathrm{Tr}\left(e^{-\beta\left(H^{tot} - \sum_{\gamma=1}^{c} \mu_{\gamma} Q_{\gamma}^{tot}\right)}\right)$.

Define $\rho_{NATS}^{(j)}$ and ρ_{NATS}^{avg} analogously to $\rho_{can}^{(j)}$ and ρ_{can}^{avg}.

Our argument concerns multiple distance measures. Let O denote an arbitrary observable defined on an arbitrary Hilbert space. The Schatten p-norm of O is $||O||_p := [\mathrm{Tr}(|O|^p)]^{1/p}$, wherein $|O| := \sqrt{O^{\dagger}O}$ and $p \in [0, \infty)$. The limit as $p \to \infty$ yields the operator norm: $\lim_{p\to\infty} ||O||_p =: ||O||_{op}$. Let ρ and σ denote operators defined on an arbitrary Hilbert space. The Schatten p-distance between the states is $||\rho - \sigma||_p$. The trace distance is $\mathcal{D}_{tr}(\rho, \sigma) = \frac{1}{2}||\rho - \sigma||_1$.

2. Lower bounds on distances between thermal states

We now formalize the result.

Theorem 1. *Let the setup and definitions be as in Sec. F 1. Consider the distance from the average NATS to the*

average canonical state. Measured with the Schatten 1-distance or the relative entropy, this distance obeys the lower bound

$$D\left(\rho_{\text{NATS}}^{\text{avg}} || \rho_{\text{can}}^{\text{avg}}\right) \geq \mathcal{D}_{\text{tr}}\left(\rho_{\text{NATS}}^{\text{avg}}, \rho_{\text{can}}^{\text{avg}}\right) \geq \frac{|q_\gamma|}{\left\|Q_\gamma^{(j)}\right\|_{\text{op}}} > 0,$$

(F7)

for an arbitrary $j = 1, 2, \ldots, N$. ρ_{can} can be replaced with any grand canonical state that commutes with V.

The bound does not depend on N and so holds in the thermodynamic limit.

Proof. The proof has the following outline. First, we calculate the expectation value of $Q_\gamma^{(1)}$ in $\rho_{\text{NATS}}^{\text{avg}}$; the result is q_γ. Second, we show using V that the expectation value in $\rho_{\text{can}}^{\text{avg}}$ vanishes. Because the two expectation values differ, a nonzero Schatten 1-distance separates the states. The Schatten 1-distance lower bounds the relative entropy via Pinsker's inequality.

$Q_\gamma^{(1)}$ has an expectation value, in the average NATS state, of

$$\text{Tr}(Q_\gamma^{(1)} \rho_{\text{NATS}}^{\text{avg}})$$

$$= \frac{1}{N} \sum_{j=1}^{N} \text{Tr}\left(Q_\gamma^{(1)} \mathcal{T}_j \left(\rho_{\text{NATS}}^{(j,j\oplus 1,\ldots,j\oplus\tau\ominus 1)}\right)\right)$$

(F8)

$$= \frac{1}{N} \sum_{j=1}^{N} \text{Tr}\left(Q_\gamma^{(j)} \rho_{\text{NATS}}^{(j)}\right)$$

(F9)

$$= \frac{1}{N} \text{Tr}\left(\left[\sum_{j=1}^{N} \mathbb{1}^{\otimes(j-1)} \otimes Q_\gamma^{(j)} \otimes \mathbb{1}^{\otimes(N-j)}\right]\left[\bigotimes_{k=1}^{N} \rho_{\text{NATS}}^{(k)}\right]\right)$$

(F10)

$$= \frac{1}{N} \text{Tr}\left(Q_\gamma^{\text{tot}} \rho_{\text{NATS}}^{\text{tot}}\right)$$

(F11)

$$= q_\gamma.$$

(F12)

Equation (F9) follows from the definition of $\mathcal{T}_j$. Equation (F12) follows Eq. (F6).

Next, we show that the analogous canonical expectation value vanishes. We begin with the global expectation value $\text{Tr}(Q_\gamma^{\text{tot}} e^{-\beta H^{\text{tot}}})/Z_{\text{can}}^{\text{tot}}$. By Eq. (F1), we can replace the Q_γ^{tot} with $-VQ_\gamma^{\text{tot}}V^\dagger$. We then invoke the cyclicality of the trace:

$$\text{Tr}\left(Q_\gamma^{\text{tot}} e^{-\beta H^{\text{tot}}}\right)/Z_{\text{can}}^{\text{tot}} = -\text{Tr}\left(\left[VQ_\gamma^{\text{tot}}V^\dagger\right] e^{-\beta H^{\text{tot}}}\right)/Z_{\text{can}}^{\text{tot}}$$

(F13)

$$= -\text{Tr}\left(Q_\gamma^{\text{tot}} \left[V^\dagger e^{-\beta H^{\text{tot}}} V\right]\right)/Z_{\text{can}}^{\text{tot}}$$

(F14)

$$= -\text{Tr}\left(Q_\gamma^{\text{tot}} e^{-\beta H^{\text{tot}}}\right)/Z_{\text{can}}^{\text{tot}}.$$

(F15)

Equation (F15) follows from $[V, H^{\text{tot}}] = 0$. Let us compare the beginning and end of Eqs. (F13)–(F15). The expectation value $\text{Tr}\left(Q_\gamma^{\text{tot}} e^{-\beta H^{\text{tot}}}\right)/Z_{\text{can}}^{\text{tot}}$ equals its negative and so vanishes. We can reexpress the null-expectation value in terms of the average canonical state:

$$0 = \sum_{j=1}^{N} \text{Tr}\left(Q_\gamma^{\text{tot}} e^{-\beta H^{\text{tot}}}\right)/Z_{\text{can}}^{\text{tot}}$$

(F16)

$$= \sum_{j=1}^{N} \text{Tr}\left(\left[\mathbb{1}^{\otimes(j-1)} \otimes Q_\gamma^{(j)} \otimes \mathbb{1}^{\otimes(N-j)}\right] e^{-\beta H^{\text{tot}}}\right)/Z_{\text{can}}^{\text{tot}}$$

(F17)

$$= \sum_{j=1}^{N} \text{Tr}\left(Q_\gamma^{(j)} \text{Tr}_{\bar{j}}\left(e^{-\beta H^{\text{tot}}}\right)\right)/Z_{\text{can}}^{\text{tot}}$$

(F18)

$$= \sum_{j=1}^{N} \text{Tr}_j\left(Q_\gamma^{(j)} \rho_{\text{can}}^{(j)}\right)$$

(F19)

$$= \sum_{j=1}^{N} \text{Tr}\left(Q_\gamma^{(1)} \mathcal{T}_j\left(\rho_{\text{can}}^{(j,j\oplus 1,\ldots,j\oplus\tau\ominus 1)}\right)\right)$$

(F20)

$$= \text{Tr}\left(Q_\gamma^{(1)} \rho_{\text{can}}^{\text{avg}}\right).$$

(F21)

Equations (F19) and (F20) are analogous to Eqs. (F9) and (F8).

We have calculated two expectation values of Q_γ^1, one in $\rho_{\text{NATS}}^{\text{avg}}$ and one in $\rho_{\text{can}}^{\text{avg}}$. The two expectation values differ, by Eqs. (F16), (F21), and (F12):

$$\left|\text{Tr}\left(Q_\gamma^{(1)} \rho_{\text{NATS}}^{\text{avg}}\right) - \text{Tr}\left(Q_\gamma^{(1)} \rho_{\text{can}}^{\text{avg}}\right)\right| = |q_\gamma| > 0.$$

(F22)

We can relate the absolute difference, given in Eq. (F22), to the trace distance. Let ρ and σ denote quantum states defined on an arbitrary Hilbert space. The interstate distance equals a supremum over observables O defined on the same space [82, Lemma 9.1.1]:

$$\mathcal{D}_{\text{tr}}(\rho, \sigma) = \sup_{O\,:\,||O||_{\text{op}} \leq 1} \{|\text{Tr}(\rho O) - \text{Tr}(\sigma O)|\}.$$

(F23)

Let $\rho = \rho_{\text{NATS}}^{\text{avg}}$ and $\sigma = \rho_{\text{can}}^{\text{avg}}$. The operator $Q_\gamma^{(1)}/||Q_\gamma^{(1)}||_{\text{op}}$ is one normalized O. Therefore, by Eq. (F22), $|q_\gamma|/||Q_\gamma^{(1)}||_{\text{op}}$ lower bounds the supremum in Eq. (F23). The superscript (1) can be replaced with (j), due to translation invariance in the $\mathcal{T}_j$ argument. Hence $\mathcal{D}_{\text{tr}}(\rho_{\text{NATS}}^{\text{avg}}, \rho_{\text{can}}^{\text{avg}}) \geq |q_\gamma|/||Q_\gamma^{(j)}||_{\text{op}} > 0$. The final inequality follows from (i) the assumption in Eq. (F2) and (ii) the finiteness of the single-subsystem $||Q_\gamma^{(j)}||_{\text{op}}$. The first inequality in Eq. (F7) follows via Pinsker's inequality: for states ρ and

σ, $D(\rho||\sigma) \geq \mathcal{D}_{\text{tr}}(\rho, \sigma)$. This proof remains true if ρ_{GC} replaces ρ_{can} and $[\rho_{\text{GC}}, V] = 0$. ∎

3. Realization in trapped-ion experiment

The general setup of Appendix F 1 can be realized in the trapped-ion experiment of the main text. In the simplest realization, $Q_\gamma = \sigma_x$. The unitary $V = \sigma_z^{\otimes N}$:

$$V\sigma_x^{\text{tot}} V^\dagger = \sigma_z^{\otimes N} \left(\sum_{j=1}^{N} \sigma_x^{(j)} \right) \sigma_z^{\otimes N} = \sum_{j=1}^{N} (-\sigma_x^{(j)}) = -\sigma_x^{\text{tot}}.$$

$$(\text{F24})$$

The initial state is $|\psi_0\rangle = |x+, y+, z+\rangle^{\otimes N/3}$, so $\langle\psi_0|\sigma_x^{\text{tot}} |\psi_0\rangle \propto N$ and the state is invariant under translations through $\tau = 3$ sites. Define $\rho_{\text{GC}}^{\text{tot}} := \exp\left(-\beta \left[H^{\text{tot}} - \mu_z S_z^{\text{tot}}\right]\right)/Z_{\text{GC}}^{\text{tot}}$. The effective chemical potential μ_z is defined as in the main text and $Z_{\text{GC}}^{\text{tot}}$ normalizes the state. $\rho_{\text{GC}}^{\text{tot}}$ can replace the canonical state in Eq. (F7).

The mapping just described is conceptually simple. However, we find analytically that another mapping achieves the tightest bound in Eq. (F7): $1/\sqrt{3}\left(\sigma_x + \sigma_y + \sigma_z\right)$, and $V = \left[1/\sqrt{6}(2\sigma_x - \sigma_y - \sigma_z)\right]^{\otimes N}$. (Alternatively, the σ_γs in V can be permuted in any way.)

APPENDIX G: SPATIOTEMPORAL FLUCTUATIONS IN DISTANCES OF STATES TO THE NON-ABELIAN THERMAL STATE

Figure 5 shows the experimentally observed fluctuations, across space and time, of the relative entropy to the NATS. The chain consists of $N = 21$ ions. The state of every ion pair approaches the NATS in time. However, nonuniformity remains; edge pairs thermalize more slowly due to edge effects, while the central pairs thermalize more quickly.

APPENDIX H: DERIVATIONS OF TROTTER SEQUENCES

The evolution implemented differs from evolution under the Heisenberg Hamiltonian given in Eq. (3) for three reasons. First, the Heisenberg Hamiltonian is Trotter approximated. Second, parts of the Trotter approximation are simulated via native interactions dressed with rotations. Third, we reduce decoherence via dynamical decoupling. Here, we derive the experimental pulse sequence. We review parts of the setup and introduce notation in Appendix H 1. In Appendix H 2, we detail the two errors against which the pulse sequence protects. We derive the pulse sequence in Appendix H 3. Appendix H 4 extends the derivation from the Heisenberg evolution to the XY model given in Eq. (7).
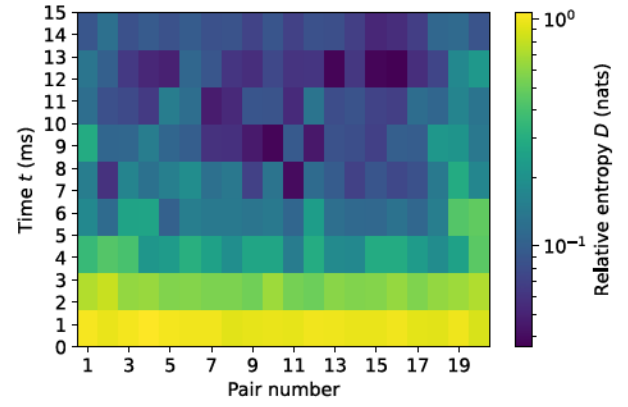

FIG. 5. The relative entropy to the NATS for each qubit pair, as a function of time. The spatiotemporal fluctuations show that different qubit pairs thermalize to different extents. The chain consists of $N = 21$ ions.

1. Quick review of setup and notation

We break a length-t time interval into N_T steps of length $t/N_T =: \Delta t$ each. We aim to simulate the Heisenberg Hamiltonian given in Eq. (3), the $J_0/|j - k|^\alpha$ of which we sometimes denote here by $J_{j,k}$. H_{Heis} generates the family of unitaries $U_{\text{Heis}}(t) := e^{-iH_{\text{Heis}}t}$. To effect this family, we leverage single-axis Hamiltonians

$$H_{\gamma\gamma} := \sum_{j=1}^{N} \sum_{k>j} J_{j,k} \, \sigma_\gamma^{(j)} \sigma_\gamma^{(k)}. \qquad (\text{H1})$$

H_{xx} and H_{yy} are native to the experimental platform. The Hamiltonians in Eq. (H1) generate the unitaries $e^{-iH_{\gamma\gamma}\Delta t} =: U_{\gamma\gamma}$. We interleave the interaction with rotations $R_\gamma := \exp\left(-i\,\pi/4\,\sigma_\gamma^{\text{tot}}\right)$, for $\gamma = x, y, z$. We denote the single-qubit identity operator by $\mathbb{1}$.

2. Two sources of error

Our pulse sequence combats detuning and rotation errors. The detuning error manifests as an undesired term that creeps into the Hamiltonian in Eq. (3). Proportional to σ_z^{tot}, the term represents an external magnetic field. We protect against the detuning error with dynamical decoupling: the detuning error undesirably rotates the state of each ion about the z axis. We apply a π pulse about the x axis, reflecting the state through the x-y plane. The state then precesses about the z axis oppositely, undoing the earlier precession. Another π pulse undoes the reflection.

The second error plagues the engineered rotations: a qubit may rotate too little or too much, because the ion string is not quite uniformly illuminated. We therefore replace certain rotations R_γ with rotations $R_\gamma^\dagger$. An ion may rotate too much while undergoing R_γ but, while undergoing $R_\gamma^\dagger$, rotates through the same angle oppositely. The excess rotations cancel.

3. Derivation of Trotter sequence

First, we divvy up the Heisenberg evolution into steps. Then, we introduce rotations that enable dynamical decoupling. We Trotter approximate a Heisenberg step in two ways. Alternating the two Trotter approximations across a pulse sequence mitigates rotation errors. Engineering of robust Hamiltonians has recently been demonstrated for analog simulations [83,84] and digital circuits [85].

To simulate the Heisenberg Hamiltonian for a time t, we evolve for N_T length-Δt time steps: $U_{\text{Heis}}(t) = [U_{\text{Heis}}(\Delta t)]^{N_T}$. To facilitate dynamical decoupling, we insert an identity operator on the left: $U_{\text{Heis}}(t) = \mathbb{1}^{\otimes N}[U_{\text{Heis}}(\Delta t)]^{N_T}$. We decompose the $\mathbb{1}^{\otimes N}$ into rotations about the z axis. How this decomposition facilitates dynamical decoupling is not yet obvious, as the rotations commute with the detuning expression. Later, though, we will commute some of the rotations across interaction unitaries. The commutation will transform the z rotations into R_x rotations. For now, we decompose the $\mathbb{1}^{\otimes N}$ in two ways:

$$U_{\text{Heis}}(t) = (R_z^\dagger)^{N_T}(R_z)^{N_T}[U_{\text{Heis}}(\Delta t)]^{N_T} \tag{H2}$$

$$= (R_z)^{N_T}(R_z^\dagger)^{N_T}[U_{\text{Heis}}(\Delta t)]^{N_T}. \tag{H3}$$

We implement the right-hand side of Eq. (H2) during half the protocol and, during the other half, we implement Eq. (H3). This alternation mitigates rotation errors.

Let us analyze Eq. (H2), then Eq. (H3). R_z commutes with $U_{\text{Heis}}(\Delta t)$ because the Heisenberg Hamiltonian conserves σ_z^{tot}: $[H_{\text{Heis}}, \sigma_z^{\text{tot}}] = 0$ implies that $[U_{\text{Heis}}(\Delta t), R_z] = 0$. The R_zs of Eq. (H2) can therefore move inside the square brackets:

$$U_{\text{Heis}}(t) = (R_z^\dagger)^{N_T} [R_z U_{\text{Heis}}(\Delta t)]^{N_T}. \tag{H4}$$

We Trotter approximate the short Heisenberg evolution as

$$U_{\text{Heis}}(\Delta t) \approx U_{yy} U_{zz} U_{xx}. \tag{H5}$$

The ordering of the directions is arbitrary.

We substitute into Eq. (H4) and rewrite the bracketed factor, pursuing three goals. First, the U_{zz} is not native to our platform. We therefore simulate it with $R_y^\dagger U_{xx} R_y$. Second, one R_x must end up amidst the $U_{\gamma\gamma}$s. Two blocks of $U_{\gamma\gamma}$s, each containing an R_x, will consequently effect one π pulse. Composing these π pulses will effect dynamical decoupling. Third, any other, stray R_γs must be arranged symmetrically on either side of the $U_{\gamma\gamma}$s, as explained below.

Let us replace the U_{zz} in Eq. (H5) with $R_y^\dagger U_{xx} R_y$ [86]. The $R_y^\dagger$ commutes across the U_{yy}:

$$R_z U_{yy} U_{zz} U_{xx} = R_z U_{yy} (R_y^\dagger U_{xx} R_y) U_{xx} \tag{H6}$$

$$= R_z R_y^\dagger U_{yy} U_{xx} R_y U_{xx}. \tag{H7}$$

We have eliminated the U_{zz}. Similarly eliminating the R_z will prove useful, so we invoke $R_z = R_y^\dagger R_x R_y$:

$$R_z U_{yy} U_{zz} U_{xx} = (R_y^\dagger R_x \cancel{R_y}) \cancel{R_y^\dagger} U_{yy} U_{xx} R_y U_{xx} \tag{H8}$$

$$= (R_y^\dagger R_x) U_{yy} U_{xx} R_y U_{xx}. \tag{H9}$$

We will benefit from complementing the $R_y^\dagger R_x$ with a mirror image $(R_y^\dagger R_x)^\dagger = R_x^\dagger R_y$ on the right. We will implement $R_z U_{yy} U_{zz} U_{xx}$ many times and instances of the left-hand $R_y^\dagger R_x$ will cancel instances of the right-hand $R_x^\dagger R_y$. Therefore, we insert $\mathbb{1}^{\otimes N} = R_y^\dagger R_x R_x^\dagger R_y$ into the right-hand side of Eq. (H8):

$$R_z U_{yy} U_{zz} U_{xx} = (R_y^\dagger R_x) U_{yy} U_{xx} \underbrace{R_y U_{xx} (R_y^\dagger}_{=U_{zz}} R_x R_x^\dagger R_y). \tag{H10}$$

Again, U_{zz} is not native to our platform. We therefore commute the R_x across the U_{zz}, invoking $R_x^\dagger U_{zz} R_x = U_{yy}$:

$$R_z U_{yy} U_{zz} U_{xx} = (R_y^\dagger R_x) \underbrace{U_{yy} U_{xx} R_x U_{yy}}_{=:E_+} (R_x^\dagger R_y). \tag{H11}$$

The final expression has the sought-after form. We substitute into Eq. (H5), then into Eq. (H4), and then cancel rotations: $U_{\text{Heis}}(t) \approx (R_z^\dagger)^{N_T}(R_y^\dagger R_x) (E_+)^{N_T}(R_x^\dagger R_y)$.

Suppose that $N_T = 4$. The E_+s, containing four R_xs in total, implement two π pulses—one round of dynamical decoupling. Furthermore, $(R_z^\dagger)^4 = (-1)^{N_T}\mathbb{1}^{\otimes N}$, so

$$U_{\text{Heis}}(4\Delta t) \approx (R_z^\dagger)^4 (R_y^\dagger R_x) (E_+)^4 (R_x^\dagger R_y) \tag{H12}$$

$$= (-1)^N (R_y^\dagger R_x) (E_+)^4 (R_x^\dagger R_y). \tag{H13}$$

Now, let $N_T \gg 4$, as in the experiment. After one round of dynamical decoupling, to mitigate the detuning error, we mitigate rotation errors. We effect four time steps with an alternative operator derived from Eq. (H3). Then, we continue alternating.

Let us derive the alternative to E_+. We shift the $R_z^\dagger$s of Eq. (H3) inside the square brackets:

$$U_{\text{Heis}}(t) = (R_z)^{N_T} [R_z^\dagger U_{\text{Heis}}(\Delta t)]^{N_T} \tag{H14}$$

$$\approx (R_z)^{N_T} [R_z^\dagger U_{yy} U_{zz} U_{xx}]^{N_T}. \tag{H15}$$

The final expression follows from Eq. (H5). The bracketed factor must end up with the $(R_y^\dagger R_x)[\dots](R_x^\dagger R_y)$ structure of Eq. (H11), so that rotations cancel between instances of Eq. (H11) and instances of the new bracketed factor. We therefore ensure that $R_y^\dagger R_x$ is on the left-hand side of the

$U^{(0)} = (U_{yy}U_{zz}U_{xx})^{N_T}, \quad U^{(1)} = (R_y^\dagger R_x)(E_+)^{N_T}(R_x^\dagger R_y), \quad U^{(1alt)} = R_y^\dagger R_x[(E_-)^4(E_+)^4]^{N_T/8} R_x^\dagger R_y \text{ for } \mathrm{mod}(N_T, 8) = 0$

$E_+ = U_{yy}U_{xx}R_x U_{yy}, \quad E_- = U_{yy}U_{xx}R_x^\dagger U_{yy}, \quad R_\alpha^{(\dagger)}... \text{positive (negative) rotation around} \quad \alpha = x, y, z$
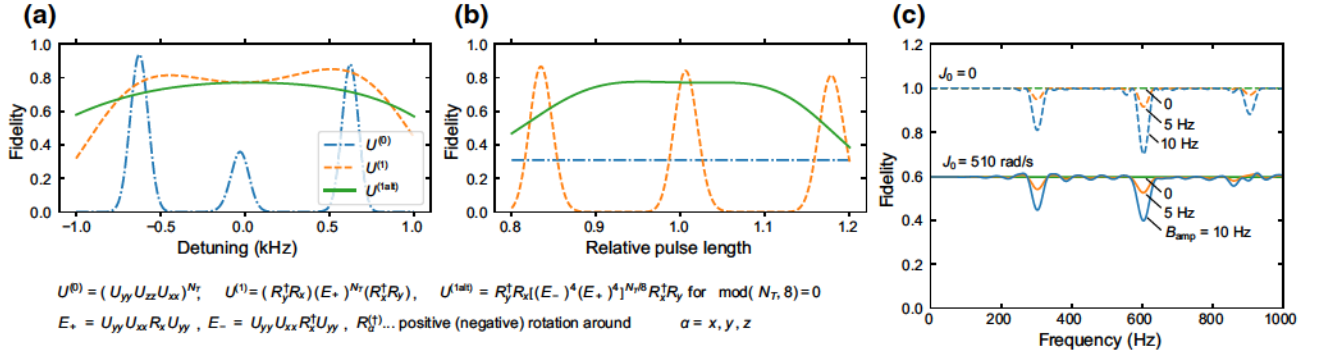
FIG. 6. Dynamical decoupling. The simulation is performed with 12 ions, a power-law approximation to the coupling, $J_0 = 510$ rad/s, $\alpha = 1.02$, and 10 ms of evolution. The fidelity compares the simulated Trotter-approximated state with the exact ideal state: $\left(\mathrm{Tr}\sqrt{\sqrt{\rho_{\mathrm{exact}}}\rho_{\mathrm{Trotter}}\sqrt{\rho_{\mathrm{exact}}}}\right)^2$. (a) The introduction of $\pi/2$ rotations into the Trotter sequence guards against detuning errors. The right-hand side (rhs) of Eq. (H5) defines the sequence $U^{(0)}$, the rhs of Eq. (H22) defines $U^{(1)}$, and the rhs of Eq. (H23) defines $U^{(1alt)}$. (b) Alternating the direction of the rotations guards against systematic rotation errors. (c) The response to oscillations of a time-varying magnetic field $\mathbf{B} = B_{\mathrm{amp}}\cos(2\pi ft)\hat{z}$, wherein $B_{\mathrm{amp}} \geq 0$ (15 ms evolution). The dynamically decoupled Trotter sequence $U^{(1alt)}$ allows the fidelity to drop. The drops occur when the frequency of the field, f, is an integer multiple of $f_1 = \frac{1}{2}(4T_{\mathrm{tot}}/N_{\mathrm{Trotter}})^{-1} = 300$ Hz. We can understand this behavior most simply when $J_0 = 0$ (top curves): the qubits do not interact, so each qubit remains in a superposition, the relative phase of which changes undesirably under $\mathbf{B}$.

factor, then propagate extraneous rotations leftward:

$$\underbrace{R_z^\dagger} \qquad U_{yy}U_{zz}U_{xx} \qquad (\mathrm{H}16)$$

$$= R_y^\dagger R_x^\dagger R_y = R_y^\dagger \mathbb{1}^{\otimes N} R_x^\dagger R_y = R_y^\dagger (R_x R_x^\dagger) R_x^\dagger R_y$$

$$= (R_y^\dagger R_x)(R_x^\dagger)^2 \underbrace{R_y U_{yy}}_{=U_{yy}R_y} U_{zz}U_{xx} \qquad (\mathrm{H}17)$$

$$= (R_y^\dagger R_x)R_x^\dagger \underbrace{R_x^\dagger U_{yy}}_{=U_{zz}R_x^\dagger} \underbrace{R_y U_{zz}}_{=U_{xx}R_y} U_{xx} \qquad (\mathrm{H}18)$$

$$= (R_y^\dagger R_x) \underbrace{R_x^\dagger U_{zz}}_{=U_{yy}R_x^\dagger} \underbrace{R_x^\dagger U_{xx}}_{=U_{xx}R_x^\dagger} \underbrace{R_y U_{xx}}_{=U_{zz}R_y} \qquad (\mathrm{H}19)$$

$$= (R_y^\dagger R_x)U_{yy} \underbrace{R_x^\dagger U_{xx}}_{=U_{xx}R_x^\dagger} \underbrace{R_x^\dagger U_{zz}}_{=U_{yy}R_x^\dagger} R_y \qquad (\mathrm{H}20)$$

$$= (R_y^\dagger R_x)\underbrace{U_{yy}U_{xx}R_x^\dagger U_{yy}}_{=:E_-}(R_x^\dagger R_y). \qquad (\mathrm{H}21)$$

By Eq. (H14), $U_{\mathrm{Heis}}(t) \approx (R_z)^{N_T}(R_y^\dagger R_x)(E_-)^{N_T}(R_x^\dagger R_y)$. Analogously to Eq. (H13),

$$U_{\mathrm{Heis}}(4\Delta t) \approx (-1)^N(R_y^\dagger R_x)(E_-)^4(R_x^\dagger R_y). \qquad (\mathrm{H}22)$$

We alternate instances of Eq. (H13) with instances of Eq. (H22) to simulate long Heisenberg evolutions. Many rotations cancel. If N_T equals an integer multiple of eight,

$$U_{\mathrm{Heis}}(t) \approx R_y^\dagger R_x\left[(E_-)^4(E_+)^4\right]^{N_T/8} R_x^\dagger R_y. \qquad (\mathrm{H}23)$$

4. Extension from Heisenberg model to XY model

In Sec. III, we experimentally compare the Heisenberg evolution with evolution under the XY model, in Eq. (7). H_{xy} generates the unitaries $U_{xy}(t) := \exp(-itH_{xy})$. We can more easily Trotterize $U_{xy}(t)$ while mitigating errors than Trotterize $U_{\mathrm{Heis}}(t)$.

As before, we divvy up the evolution into steps. Then, we Trotter approximate the steps and insert $\mathbb{1}^{\otimes N} = \left[\left(R_x^\dagger\right)^2\right]^{N_T}(R_x^2)^{N_T}$:

$$U_{xy}(t) = [U_{xy}(\Delta t)]^{N_T} \approx (U_{yy}U_{xx})^{N_T} \qquad (\mathrm{H}24)$$

$$= \left[\left(R_x^\dagger\right)^2\right]^{N_T}(R_x^2)^{N_T}(U_{yy}U_{xx})^{N_T}. \qquad (\mathrm{H}25)$$

Due to the square, R_x^2 commutes with $U_{yy}U_{xx}$:

$$R_x^2 U_{yy}U_{xx} = R_x \underbrace{R_x U_{yy}}_{=U_{zz}R_x}U_{xx} = R_x \underbrace{U_{zz}R_x U_{xx}}_{=U_{yy}R_x} \qquad (\mathrm{H}26)$$

$$= U_{yy}\underbrace{R_x^2 U_{xx}}_{=U_{xx}R_x^2} = U_{yy}U_{xx}R_x^2. \qquad (\mathrm{H}27)$$

Therefore, in Eq. (H25), we can pull the $(R_x^2)^{N_T}$ into the parentheses:

$$U_{xy}(t) = \left[\left(R_x^\dagger\right)^2\right]^{N_T}\left(R_x^2 U_{yy}U_{xx}\right)^{N_T}. \qquad (\mathrm{H}28)$$

We could commute the R_x^2 into the center of the $U_{\gamma\gamma}$s, to improve the dynamical decoupling. However, Eq. (H28) suffices; errors accumulate in only a couple of gates.
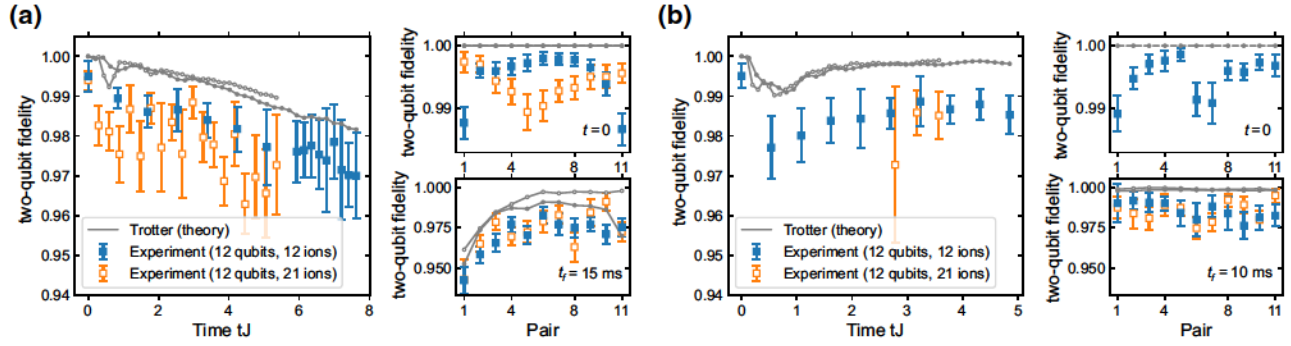
FIG. 7. The measured fidelity of the state resulting from the Trotter approximation. The fidelity of the experimentally observed state to the ideal state is averaged over ion pairs and plotted against time. The error bars indicate the standard deviation over the pairs. The smaller subplots show the fidelities, at the start and end of the evolution, to the observed states of individual ion pairs. The two types of markers represent two cases that we compare. First, we realize a 12-qubit system using a chain of only 12 ions (filled blue markers). The filled gray dots show the corresponding theoretical prediction. Second, we realize a 12-qubit system using a 21-ion chain, by hiding the extraneous ions from the interactions (empty orange markers). The open gray dots show the theoretical prediction for this case. The measurements are carried out (a) for the Trotter-approximated Heisenberg Hamiltonian and (b) for the Trotter-approximated *XY* Hamiltonian. The fidelity drops and revives at early times. This behavior results from the failure of the Trotter steps to conserve the charges of the exact Hamiltonian, leading to periodic errors.

The operator $F_+ := R_x^2 U_{yy} U_{xx}$ contains a π pulse. Therefore, we need perform F_+ only twice before implementing $F_- := (R_x^\dagger)^2$. Furthermore, $\left[\left(R_x^\dagger\right)^2\right]^2 = (-1)^N$. If N_T is a multiple of four, then $U_{xy}(t) = \left[(F_-)^2(F_+)^2\right]^{N_T/4}$.

APPENDIX I: ASSESSMENT OF NOISE-ROBUST TROTTER SEQUENCE

Appendix H describes the Trotter sequence that we engineer to alleviate errors. Here, we demonstrate the effectiveness of the sequence in numerical simulations and in the experiment. Figure 6 shows the effects of the dynamical decoupling in the parameter regime used experimentally. Constant detuning errors of up to several hundred hertz do not significantly reduce the fidelity of the time-evolved state to the ideal state, as shown in Fig. 6(a): the fidelity drops by only $< 10\%$, despite detuning errors of up to 500 Hz. Similarly, systematic rotation errors of $\pm 10\%$ affect the fidelity little [Fig. 6(b)]: the fidelity drops by 4%. If the detunings oscillate temporally [Fig. 6(c)], the robustness of the dynamical decoupling depends heavily on the oscillation frequency f. Recall that $t_f = 15$ ms denotes the temporal length of the experiment and that N_T denotes the number of Trotter steps. Consider a single-qubit state expressed as a combination of outer products of σ_z eigenstates. If f is an integer multiple of $f_1 = \frac{1}{2}(4t_f/N_T)^{-1} = 300$ Hz, the state of the qubit acquires a relative phase, reducing the fidelity to the ideal state.

Figure 7 shows the experimentally observed two-qubit fidelities $\left(\mathrm{Tr}\sqrt{\sqrt{\rho_{\mathrm{exact}}}\rho_{\mathrm{exp}}\sqrt{\rho_{\mathrm{exact}}}}\right)^2$. At $t = 0$, the fidelity is limited by imperfections in the state preparation. These imperfections result from the inhomogeneous profiles of

the global rotations (different qubits erroneously rotate by different amounts). Consequently, the initial fidelity is 0.995(4), when the Hamiltonian has the Heisenberg form given in Eq. (3) [Fig. 7(a)]. At $t > 0$, the fidelity is reduced both by Trotterization errors (gray line) and experimental imperfections. At the final time, $t = t_f$, the fidelity is 0.97(1).

Additionally, we assess the quality of the hiding operation described in Appendix A. The ion chain always contains 21 ions. However, if we wish to use fewer ions, we hide the extra ions in an extra Zeeman sublevel. To evaluate the effectiveness of this technique, we compare two cases. First, we realize a 12-qubit system with a chain of only 12 ions. Second, we realize a 12-qubit system using a 21-ion chain. Both cases yield similar fidelities in Fig. 7. However, the state-preparation errors of the two cases differ, as the preparation requires additional (hiding) operations in the second case.

The *XY*-model Trotterization [Fig. 7(b)] leads to better fidelities than the Heisenberg-model Trotterization [Fig. 7(a)]. The reason, we expect, is the greater simplicity of the *XY* Trotterization (which requires fewer steps). At early times, the fidelity of the *XY*-model Trotterization drops, then revives. This effect is visible for two-qubit subsystems. It results from the failure of the finite-length Trotter steps to conserve the charges of the exact Hamiltonian. Numerical simulations (not depicted) show that the fidelity of the total system drops at all times.

[1] A. M. Kaufman, M. E. Tai, A. Lukin, M. Rispoli, R. Schittko, P. M. Preiss, and M. Greiner, Quantum thermalization through entanglement in an isolated many-body system, Science **353**, 794 (2016).

[2] C. Neill, *et al.*, Ergodic dynamics and thermalization in an isolated quantum system, Nat. Phys. **12**, 1037 (2016).

[3] G. Clos, D. Porras, U. Warring, and T. Schaetz, Time-Resolved Observation of Thermalization in an Isolated Quantum System, Phys. Rev. Lett. **117**, 170401 (2016).

[4] Z.-Y. Zhou, G.-X. Su, J. C. Halimeh, R. Ott, H. Sun, P. Hauke, B. Yang, Z.-S. Yuan, J. Berges, and J.-W. Pan, Thermalization dynamics of a gauge theory on a quantum simulator, Science **377**, 311 (2022).

[5] M. Lostaglio, Master's thesis, Imperial College London (2014).

[6] N. Yunger Halpern, Beyond heat baths II: Framework for generalized thermodynamic resource theories, J. Phys. A: Math. Theor. **51**, 094001 (2018).

[7] Y. Guryanova, S. Popescu, A. J. Short, R. Silva, and P. Skrzypczyk, Thermodynamics of quantum systems with multiple conserved quantities, Nat. Commun. **7**, 12049 (2016).

[8] N. Yunger Halpern, P. Faist, J. Oppenheim, and A. Winter, Microcanonical and resource-theoretic derivations of the thermal state of a quantum system with noncommuting charges, Nat. Commun. **7**, 12051 (2016).

[9] M. Lostaglio, D. Jennings, and T. Rudolph, Thermodynamic resource theories, non-commutativity and maximum entropy principles, New J. Phys. **19**, 043008 (2017).

[10] C. Sparaciari, L. Del Rio, C. M. Scandolo, P. Faist, and J. Oppenheim, The first law of general quantum resource theories, Quantum **4**, 259 (2020).

[11] Z. B. Khanian, From quantum source compression to quantum thermodynamics (2020), ArXiv:2012.14143.

[12] Z. B. Khanian, M. N. Bera, A. Riera, M. Lewenstein, and A. Winter, Resource theory of heat and work with non-commuting charges: Yet another new foundation of thermodynamics (2020), ArXiv:2011.08020.

[13] G. Gour, D. Jennings, F. Buscemi, R. Duan, and I. Marvian, Quantum majorization and a complete set of entropic conditions for quantum thermodynamics, Nat. Commun. **9**, 5352 (2018).

[14] G. Manzano, J. M. R. Parrondo, and G. T. Landi, Non-Abelian Quantum Transport and Thermosqueezing Effects, PRX Quantum **3**, 010304 (2022).

[15] S. Popescu, A. B. Sainz, A. J. Short, and A. Winter, Quantum reference frames and their applications to thermodynamics, Philos. Trans. R. Soc. A: Math. Phys. Eng. Sci. **376**, 20180111 (2018).

[16] S. Popescu, A. B. Sainz, A. J. Short, and A. Winter, Reference Frames Which Separately Store Noncommuting Conserved Quantities, Phys. Rev. Lett. **125**, 090601 (2020).

[17] K. Ito and M. Hayashi, Optimal performance of generalized heat engines with finite-size baths of arbitrary multiple conserved quantities beyond independent-and-identical-distribution scaling, Phys. Rev. E **97**, 012129 (2018).

[18] M. N. Bera, A. Riera, M. Lewenstein, Z. B. Khanian, and A. Winter, Thermodynamics as a consequence of information conservation, Quantum **3**, 121 (2019).

[19] J. Mur-Petit, A. Relaño, R. A. Molina, and D. Jaksch, Revealing missing charges with generalised quantum fluctuation relations, Nat. Commun. **9**, 2006 (2018).

[20] G. Manzano, Squeezed thermal reservoir as a generalized equilibrium reservoir, Phys. Rev. E **98**, 042123 (2018).

[21] N. Yunger Halpern, M. E. Beverland, and A. Kalev, Noncommuting conserved charges in quantum many-body thermalization, Phys. Rev. E **101**, 042117 (2020).

[22] G. Manzano, R. Sánchez, R. Silva, G. Haack, J. B. Brask, N. Brunner, and P. P. Potts, Hybrid thermal machines: Generalized thermodynamic resources for multitasking, Phys. Rev. Res. **2**, 043302 (2020).

[23] K. Fukai, Y. Nozawa, K. Kawahara, and T. N. Ikeda, Noncommutative generalized Gibbs ensemble in isolated integrable quantum systems, Phys. Rev. Res. **2**, 033403 (2020).

[24] J. Mur-Petit, A. Relaño, R. A. Molina, and D. Jaksch, Fluctuations of work in realistic equilibrium states of quantum systems with conserved quantities (2019), ArXiv:1910.11000.

[25] M. Scandi and M. Perarnau-Llobet, Thermodynamic length in open quantum systems, Quantum **3**, 197 (2019).

[26] P. Boes, H. Wilming, J. Eisert, and R. Gallego, Statistical ensembles without typicality, Nat. Commun. **9**, 1 (2018).

[27] Y. Mitsuhashi, K. Kaneko, and T. Sagawa, Characterizing Symmetry-Protected Thermal Equilibrium by Work Extraction, Phys. Rev. X **12**, 021013 (2022).

[28] T. Croucher, J. Wright, A. R. R. Carvalho, S. M. Barnett, and J. A. Vaccaro, in *Thermodynamics in the Quantum Regime: Fundamental Aspects and New Directions*, edited by F. Binder, L. A. Correa, C. Gogolin, J. Anders, and G. Adesso (Springer International Publishing, Cham, 2018), p. 713.

[29] J. A. Vaccaro and S. M. Barnett, Information erasure without an energy cost, Proc. R. Soc. London A: Math. Phys. Eng. Sci. **467**, 1770 (2011).

[30] J. S. S. T. Wright, T. Gould, A. R. R. Carvalho, S. Bedkihal, and J. A. Vaccaro, Quantum heat engine operating between thermal and spin reservoirs, Phys. Rev. A **97**, 052104 (2018).

[31] Z. Zhang, J. Tindall, J. Mur-Petit, D. Jaksch, and B. Buča, Stationary state degeneracy of open quantum systems with non-Abelian symmetries, J. Phys. A Math. Gen. **53**, 215304 (2020).

[32] M. Medenjak, B. Buča, and D. Jaksch, Isolated Heisenberg magnet as a quantum time crystal, Phys. Rev. B **102**, 041117(R) (2020).

[33] N. Yunger Halpern and S. Majidy, How to build Hamiltonians that transport noncommuting charges in quantum thermodynamics, npj Quantum Inf. **8**, 1 (2022).

[34] T. Croucher and J. A. Vaccaro, Memory erasure with finite-sized spin reservoir (2021), ArXiv:2111.10930.

[35] I. Marvian, H. Liu, and A. Hulse, Qudit circuits with SU(d) symmetry: Locality imposes additional conservation laws (2021), ArXiv:2105.12877.

[36] I. Marvian, H. Liu, and A. Hulse, Rotationally-invariant circuits: Universality with the exchange interaction and two ancilla qubits (2022), ArXiv:2202.01963.

[37] A. F. Ducuara, Ph.D. thesis, School of Physics, University of Bristol (2022).

[38] C. Murthy, A. Babakhani, F. Iniguez, M. Srednicki, and N. Yunger Halpern, Non-Abelian eigenstate thermalization hypothesis (2022), arXiv, ArXiv:2206.05310.

[39] S. Majidy, A. Lasek, D. A. Huse, and N. Y. Halpern, Non-Abelian symmetry can increase entanglement entropy (2022), arXiv preprint ArXiv:2209.14303.

[40] Á. L. Corps and A. Relaño, Theory of dynamical phase transitions in collective quantum systems (2022), arXiv e-prints, ArXiv:2205.03443.

[41] N. Yunger Halpern and J. M. Renes, Beyond heat baths: Generalized resource theories for small-scale thermodynamics, Phys. Rev. E **93**, 022126 (2016).

[42] J. M. Deutsch, Quantum statistical mechanics in a closed system, Phys. Rev. A **43**, 2046 (1991).

[43] M. Srednicki, Chaos and quantum thermalization, Phys. Rev. E **50**, 888 (1994).

[44] M. Rigol, V. Dunjko, and M. Olshanii, Thermalization and its mechanism for generic isolated quantum systems, Nature **452**, 854 (2008).

[45] E. T. Jaynes, Information theory and statistical mechanics II, Phys. Rev. **108**, 171 (1957).

[46] M. Rigol, Breakdown of Thermalization in Finite One-Dimensional Systems, Phys. Rev. Lett. **103**, 100403 (2009).

[47] M. Rigol, V. Dunjko, V. Yurovsky, and M. Olshanii, Relaxation in a Completely Integrable Many-Body Quantum System: An *Ab Initio* Study of the Dynamics of the Highly Excited States of 1D Lattice Hard-Core Bosons, Phys. Rev. Lett. **98**, 050405 (2007).

[48] L. Vidmar and M. Rigol, Generalized Gibbs ensemble in integrable lattice models, J. Stat. Mech.: Theory Exp. **2016**, 064007 (2016).

[49] L. D. Landau and E. M. Lifshitz, *Statistical Physics: Part 1* (Butterworth-Heinemann, Oxford, 1980).

[50] L. Viola, S. Lloyd, and E. Knill, Universal Control of Decoupled Quantum Systems, Phys. Rev. Lett. **83**, 4888 (1999).

[51] E. Jané, G. Vidal, W. Dür, P. Zoller, and J. I. Cirac, Simulation of quantum dynamics with quantum optical systems, Quantum Inf. Comput. **3**, 15 (2003).

[52] B. P. Lanyon, C. Hempel, D. Nigg, M. Müller, R. Gerritsma, F. Zähringer, P. Schindler, J. T. Barreiro, M. Rambach, G. Kirchmair, M. Hennrich, P. Zoller, R. Blatt, and C. F. Roos, Universal digital quantum simulations with trapped ions, Science **334**, 57 (2011).

[53] Y. Salathé, M. Mondal, M. Oppliger, J. Heinsoo, P. Kurpiers, A. Potočnik, A. Mezzacapo, U. Las Heras, L. Lamata, E. Solano, S. Filipp, and A. Wallraff, Digital Quantum Simulation of Spin Models with Circuit Quantum Electrodynamics, Phys. Rev. X **5**, 021027 (2015).

[54] S. Geier, N. Thaicharoen, C. Hainaut, T. Franz, A. Salzinger, A. Tebben, D. Grimshandl, G. Zürn, and M. Weidemüller, Floquet Hamiltonian engineering of an isolated many-body spin system, Science **374**, 1149 (2021).

[55] P. Scholl, H. J. Williams, G. Bornet, F. Wallner, D. Barredo, L. Henriet, A. Signoles, C. Hainaut, T. Franz, S. Geier, A. Tebben, A. Salzinger, G. Zürn, T. Lahaye, M. Weidemüller, and A. Browaeys, Microwave Engineering of Programmable *XXZ* Hamiltonians in Arrays of Rydberg Atoms, PRX Quantum **3**, 020303 (2022).

[56] D. Huse, private communication (2021).

[57] F. Monteiro, M. Tezuka, A. Altland, D. A. Huse, and T. Micklitz, Quantum Ergodicity in the Many-Body Localization Problem, Phys. Rev. Lett. **127**, 030601 (2021).

[58] T. Langen, S. Erne, R. Geiger, B. Rauer, T. Schweigler, M. Kuhnert, W. Rohringer, I. E. Mazets, T. Gasenzer, and J. Schmiedmayer, Experimental observation of a generalized Gibbs ensemble, Science **348**, 207 (2015).

[59] F. Kranzl, M. K. Joshi, C. Maier, T. Brydges, J. Franke, R. Blatt, and C. F. Roos, Controlling long ion strings for quantum simulation and precision measurements, Phys. Rev. A **105**, 052426 (2022).

[60] Long-range interactions are practical here because they internally thermalize the quantum many-body system rapidly. The interaction time can therefore be short, giving the system little time to decohere. Short-range interactions have been shown numerically to induce thermalization to near the NATS [21].

[61] D. Porras and J. I. Cirac, Effective Quantum Spin Systems with Trapped Ions, Phys. Rev. Lett. **92**, 207901 (2004).

[62] L. D'Alessio, Y. Kafri, A. Polkovnikov, and M. Rigol, From quantum chaos and eigenstate thermalization to statistical mechanics and thermodynamics, Adv. Phys. **65**, 239 (2016).

[63] N. Agmon, Y. Alhassid, and R. Levine, An algorithm for finding the distribution of maximal entropy, J. Comput. Phys. **30**, 250 (1979).

[64] Y. Alhassid, N. Agmon, and R. Levine, An upper bound for the entropy and its applications to the maximal entropy problem, Chem. Phys. Lett. **53**, 22 (1978).

[65] M. A. Nielsen and I. L. Chuang, *Quantum Computation and Quantum Information* (Cambridge University Press, Cambridge, 2010).

[66] B. Efron and R. Tibshirani, Bootstrap methods for standard errors, confidence intervals, and other measures of statistical accuracy, Stat. Sci. **1**, 54 (1986).

[67] P. Jordan and E. P. Wigner, About the Pauli exclusion principle, Z. Phys. **47**, (1928).

[68] W. Beugeling, R. Moessner, and M. Haque, Finite-size scaling of eigenstate thermalization, Phys. Rev. E **89**, 042112 (2014).

[69] Á. L. Corps and A. Relaño, Long-range level correlations in quantum systems with finite Hilbert space dimension, Phys. Rev. E **103**, 012208 (2021).

[70] We choose the evolution times such that the system effectively evolves under the *XY* and Heisenberg models for the same amount of time. We simulate the Heisenberg model by repeating three Trotter steps (*XX*, *YY*, and *ZZ*). Therefore, during a Trotter-sequence evolution of 15 ms, the system effectively evolves under a Heisenberg model for 5 ms. Simulating the *XY* model, we repeat only two Trotter steps (*XX* and *YY*), requiring a total time of $2 \times 5 \text{ ms} = 10 \text{ ms}$.

[71] S. Birnkammer, A. Bohrdt, F. Grusdt, and M. Knap, Characterizing topological excitations of a long-range Heisenberg model with trapped ions, Phys. Rev. B **105**, L241103 (2022).

[72] N. Mueller, T. V. Zache, and R. Ott, Thermalization of Gauge Theories from Their Entanglement Spectrum, Phys. Rev. Lett. **129**, 011601 (2022).

[73] M. K. Joshi, A. Fabre, C. Maier, T. Brydges, D. Kiesenhofer, H. Hainzer, R. Blatt, and C. F. Roos, Polarization-gradient cooling of 1D and 2D ion Coulomb crystals, New. J. Phys. **22**, 103013 (2020).

[74] P. Jurcevic, B. P. Lanyon, P. Hauke, C. Hempel, P. Zoller, R. Blatt, and C. F. Roos, Quasiparticle engineering and entanglement propagation in a quantum many-body system, Nature **511**, 202 (2014).

[75] T. Graß and M. Lewenstein, Trapped-ion quantum simulation of tunable-range Heisenberg chains, EPJ Quantum Technol. **1**, 8 (2014).

[76] S. Lloyd, Universal quantum simulators, Science **273**, 1073 (1996).

[77] T. Brydges, A. Elben, P. Jurcevic, B. Vermersch, C. Maier, B. P. Lanyon, P. Zoller, R. Blatt, and C. F. Roos, Probing Rényi entanglement entropy via randomized measurements, Science **364**, 260 (2019).

[78] M. K. Joshi, F. Kranzl, A. Schuckert, I. Lovas, C. Maier, R. Blatt, M. Knap, and C. F. Roos, Observing emergent hydrodynamics in a long-range quantum magnet, Science **376**, 720 (2022).

[79] M. Ježek, J. Fiurášek, and Z. c. v. Hradil, Quantum inference of states and processes, Phys. Rev. A **68**, 012305 (2003).

[80] R. Meyer, C. Musco, C. Musco, and D. Woodruff, Hutch++: Optimal stochastic trace estimation (2021), p. 142.

[81] We thank Ignacio Cirac for framing this argument.

[82] M. M. Wilde, From classical to quantum Shannon theory (2011), ArXiv:1106.1445.

[83] J. Choi, H. Zhou, H. S. Knowles, R. Landig, S. Choi, and M. D. Lukin, Robust Dynamic Hamiltonian Engineering of Many-Body Spin Systems, Phys. Rev. X **10**, 031002 (2020).

[84] W. Morong, K. Collins, A. De, E. Stavropoulos, T. You, and C. Monroe, Engineering dynamically decoupled quantum simulations with trapped ions (2022), arXiv preprint ArXiv:2209.05509.

[85] B. Zhang, S. Majumder, P. H. Leung, S. Crain, Y. Wang, C. Fang, D. M. Debroy, J. Kim, and K. R. Brown, Hidden Inverses: Coherent Error Cancellation at the Circuit Level, Phys. Rev. Appl. **17**, 034074 (2022).

[86] One can prove the equality of the expressions by writing out the Taylor series for $U_{xx} = \exp(i\Delta t H_{xx})$, conjugating each term with the rotations, invoking the Euler decomposition $R_y = \cos(\pi/4)\mathbb{1}^{\otimes N} - i\sin(\pi/4)\sigma_y^{\text{tot}}$, multiplying out, and invoking $\sigma_\lambda \sigma_\nu = i\varepsilon_{\lambda\nu\xi}\sigma_\xi$. The result is the Taylor series for U_{zz}.